THE UNIVERSITY OF CHICAGO

STRESS AND STRAIN DESIGN IN SELF-ASSEMBLED NANOPARTICLE MEMBRANES

A DISSERTATION SUBMITTED TO

THE FACULTY OF THE DIVISION OF THE PHYSICAL SCIENCES

IN CANDIDACY FOR THE DEGREE OF

DOCTOR OF PHILOSOPHY

DEPARTMENT OF PHYSICS

BY

YIFAN WANG

CHICAGO, ILLINOIS

DECEMBER 2016

TABLE OF CONTENTS

LIST OF FIGURES

ACKOWLEDGMENTS

I would like to express deepest gratitude to my Ph.D. advisor, Prof. Heinrich Jaeger, for his full support and expert guidance, without which this work would not have been possible. During all my years in Heinrich's lab, I learned a tremendous amount from him to become an independent researcher, a good collaborator and an efficient project leader. His enthusiasm for science and great personality has made the Jaeger Lab a perfect place to become a scientist.

I thank Xiao-Min Lin for his generous help and insightful discussions on my research projects. I would also like to thank Jianhui Liao, Pongsakorn Kanjanaboos, Efi Efrati, Sean McBride and Edward Barry for their collaborations, also teaching me useful techniques during my Ph.D. work.

I would particularly like to thank Qiti Guo, Justin Jureller and Yimei Chen for training and helping me on the research facilities, my projects would not have been possible without their technical supports and advices.

I thank my Ph.D. committee members: Thomas Witten, Dmitri Talapin and Abigail Vieregg for their helpful advices and guidance during my Ph.D. life. I would also like to extend my appreciation to other UChicago faculties: Sidney Nagel, Philippe Guyot-Sionnest and William Irvine for useful discussions on my projects.

Thanks to all my colleagues I met at Jaeger Lab and James Franck Institute for their friendship and great discussions, especially Qin Xu, Ivo Peters, Nicole James, Endao Han, Victor Lee,

Michelle Driscoll, Scott Waitukaitis, Sayantan Majumdar, Carlos Orellana, Kieran Murphy, Leah Roth, Vishal Soni, Noah Mitchell, Irmgard Bischofberger, Michael Boles, Igor Fedin, Dmitriy Dolzhnikov, Jelani Hannah, Remington Carey and Adam Wang for their discussions and advice.

I deeply thank my mother and father for their endless love and support I have received for the past 27 years. The unwavering faith and unconditional love of them has been the foundation for everything. I would also like to thank the rest of my family and all of my friends in Chicago for their help and support.

Finally comes to my dear wife and best friend, Stella, who has accompanied and improved me since we met in Chicago, she shared my joy and sorrow over the past 4 years and I wouldn't have achieved so much without her.

The work was supported by the NSF through grants DMR-1207204 and DMR-1508110 and through the Chicago MRSEC under NSF DMR-0820054 and DMR-1420709. Use of the Center for Nanoscale Materials, an Office of Science user facility, was supported by the U.S. Department of Energy, Office of Science, Office of Basic Energy Sciences, under contract no. DE-AC02-06CH11357.

ABSTRACT

Monolayers composed of colloidal nanoparticles, with a thickness of less than ten nanometers, have remarkable mechanical strength and can suspend over micron-sized holes to form free-standing membranes. In this thesis, I discuss experiments probing the tensile strength, bending stiffness and thermal-mechanical properties of these self-assembled nanoparticle sheets. The fracture behavior of monolayers and multilayers is investigated by attaching them to elastomer substrates which are then stretched. For different applied strain, the fracture patterns are imaged down to the scale of single particles. The resulting detailed information about the crack width distribution allows us to relate the measured overall tensile strength to the distribution of local bond strengths within a layer. I then demonstrate how these membranes can be curled up into hollow scrolls that make it possible to extract both bending and stretching moduli from indentation by atomic force microscopy. I find a bending modulus 2 orders of magnitude larger than predicted by continuum elasticity, an enhancement I associate with nonlocal microstructural constraints. Finally I explored the thermal-mechanical dependence of these membranes and found their mechanical properties can be controlled by temperature and humidity, a result of molecular scale ligand configuration changes. The membranes' ability to stretch, bend, roll up into scrolls and respond to environmental changes not only offer possibilities for a variety of applications including filtration devices and environmental sensors, but also provide better understandings of elasticity theory at a new length scale.

CHAPTER 1

INTRODUCTION

In recent years, nanoparticle-based solids using metallic or semiconducting particle cores capped with short organic ligands have attracted much interest, as they combine the specific optical, electronic or magnetic functionality of nanoparticles with the flexibility of self-assembly.[1-13] In these solids, nanoparticles serve as "artificial atoms" and a particularly interesting limit occurs when they form monolayers, i.e., when the material thickness is reduced to the size of an individual "atom". The mechanical properties of such monolayers have shown a number of remarkable features, including Young's moduli of several GPa and the ability to form freestanding membranes that can stretch across holes or trenches that are hundreds to thousands of particle diameters wide. These are fundamentally new types of two-dimensional (2D) materials in the sense that the local constituent building blocks, via the inorganic nanoparticle core, and their interactions, via the organic capping ligand, can be tuned independently with almost unlimited possibilities, a distinct advantage over other 2D systems with ordinary atoms as constituent units such as graphene.[14] In contrast to truly atomic 2D systems, in which covalent and ionic bonding provides the mechanical stability, the interactions between nanoparticles can have multiple origins and occur over a much longer length scale.[15] This introduces new possibilities and also a number of interesting questions that still remain to be answered in detail, in particular concerning the ultimate strength of such membranes; the extent to which in-plane stretching and out-of-plane bending can be related; and the thermal stability of mechanical interactions between particles. Underlying these questions is a larger issue, namely whether classical elastic membrane theory can properly describe the behavior of nanoparticle-based

solids when one or more dimensions approach the size of the constituent building blocks. In this thesis I discuss experiments that address these aspects.

Considering nanoparticle monolayer membranes as a new functional material that could have potential applications in filtration, mechanical resonators and flexible electronics,[16-18] it is important to know its fracture limit under tension.[19-24] More importantly, from knowledge about how the material fails when stretched, I can extract rich information about the interactions between particles, as mediated by the ligands. In our system, the fabrication of nanoparticle monolayers and multilayers is relatively straightforward by self-assembly at a liquid-air interface. For the experiments on tensile strength I fabricate samples via sequential layer-by-layer deposition onto an elastomer substrate. Controlled amounts of strain are applied to the nanoparticle layer by stretching the substrate. The resulting fracture patterns can be imaged down to the resolution of individual particles using a scanning electron microscope (SEM) or transmission electron microscope (TEM). Statistical analysis of the fracture patterns then gives us information about the intrinsic mechanical strength set by the ligands between nanoparticles. In comparison, it is a much more challenging task to image failure mechanisms down to the atomic level in ordinary solids using electron microscopy techniques.[25]

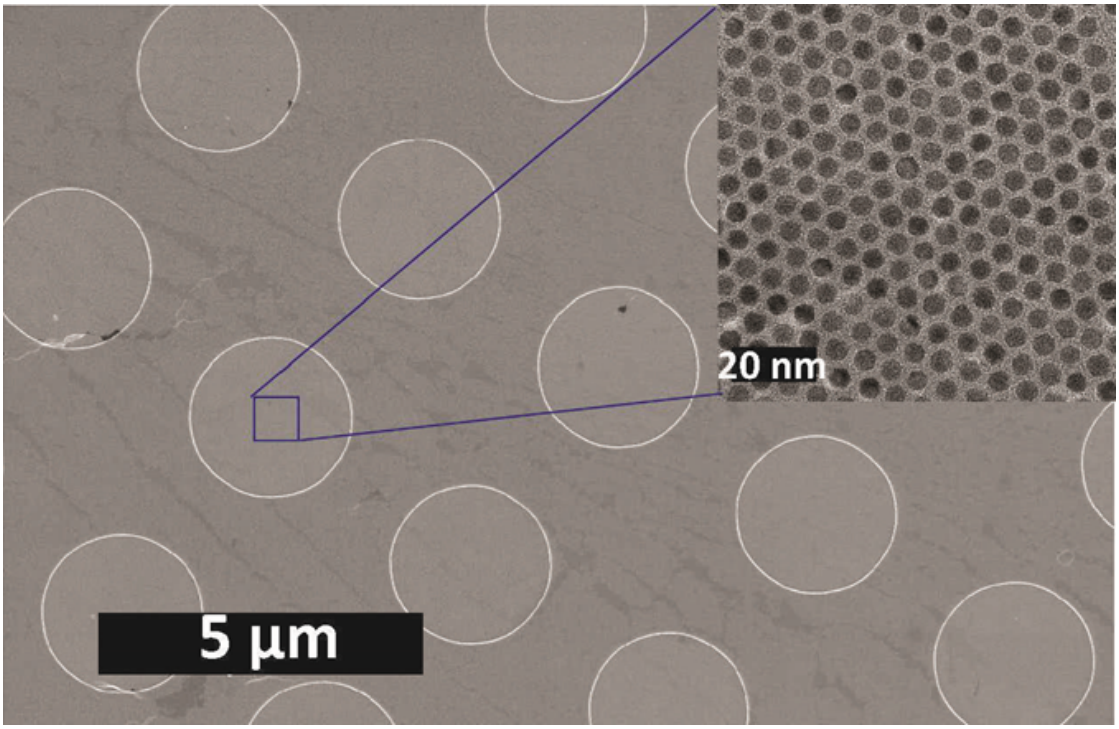

Fig 1.1 SEM image of freestanding nanoparticle monolayers on carbon-coated TEM grid with array of circular holes. Inset: zoomed-in detail of region within freestanding membrane imaged by TEM.

The ability to drape nanoparticle monolayers across holes or trenches so they form freestanding membranes provides unique opportunities for investigating the response to out-of-plane bending. We recently discovered[26] that an asymmetry develops between the two faces of gold-dodecanethiol nanoparticle layers when they are self-assembled at an air-water interface under conditions where the ligand packing density on the particle cores is lower than the maximum density. The asymmetry consists of slightly fewer ligands occupying the water-facing side of the monolayer as compared to the air-facing side. In most cases, this asymmetry by itself is not sufficient to drive spontaneous curling up of a membrane toward the side originally facing the water once the stress is relieved that keeps the membrane tautly stretched across a hole or trench. Indeed, when freestanding membranes have ripped I find portions that spontaneously have bent to either side, likely depending on the precise details of the process that caused the ripping.

However, when I use the electron beam from an electron microscope to irradiate a freestanding membrane I induce strain that greatly amplifies the asymmetry.

In this thesis, I demonstrate how this amplification effect can be used to bend sections of a nanoparticle membrane in a highly controlled manner toward the originally water-facing side, making it possible fold membranes and roll them up into three-dimensional structures: hollow nano-scrolls. While this approach offers control, it uses large exposure doses, which makes it slow and furthermore modifies the ligands through a combination of cutting and cross-linking.[27-29] Spontaneous self-rolling can be achieved by carefully adjusting the ligand concentration together with the draping and drying conditions. This produces nano-scrolls whose ligands have not been modified. Measurements of the scrolls' response to indentation then provide values for the membrane bending stiffness that can be compared directly to measurements of the stretching stiffness from prior work.[30,31] I show that the bending stiffness extracted this way is significantly larger than predicted by macroscopic continuum elastic theory. Such enhanced bending rigidity implies enhanced robustness for nanoparticle-based hollow structures, which is a desirable feature for potential applications.

In these nanoparticle membranes the nanoparticles are held together by the van der Waals attraction between surface ligands from neighboring particles. One particular interesting question arises as to how this interaction, and therefore the mechanical properties of the membranes is affected by different environmental conditions, *i.e.* variations in temperature and humidity. Previous molecular dynamic simulation results predict that the ligand layers go through a melting transition and the Young's modulus would decrease to zero[32] at ~50 °C. In our

experiments, the freestanding membranes are found to be stable up to 100-120 °C, much higher than the limiting temperature predicted from currently available simulations. A very interesting discovery is the sensitivity of the membranes to humidity in the surrounding environment, given that the ligands are nominally hydrophobic. One way to rationalize this behavior is to connect it to the change of the dielectric constant entering the van der Waals' interaction between ligands when water molecules get close. Due to the high dielectric constant of water, small changes in humidity can therefore have a significant effect.

This Thesis is organized as follows. Chapter 2 gives an overview of the fabrication procedure used to make freestanding nanoparticle monolayer membranes together with nanoparticle self-assembly and characterization techniques. Chapter 3 then describes in-plane stretching experiments of these membranes where I investigated their fracture and failure behavior and measured their fracture strength. Chapter 4 introduces methods to bend and roll these membranes into 3D structures, hollow "nanoscrolls" by utilizing a small, but significant asymmetry in the ligand shell of nanoparticles self-assembled at a water-air interface. I performed experiments on indenting these nanoparticle scrolls and obtained the membrane bending modulus for the first time, which is described in Chapter 5. In Chapter 6 of this thesis, I introduce experiments characterizing the thermal-mechanical behavior of freestanding membranes. The material stiffness and Young's moduli can be extracted by indenting the freestanding membranes with an atomic force microscope (AFM) and analyzing the resulting force-indentation curves. By conducting the measurements at different temperatures, under different environmental conditions by changing humidity, or by modifying the ligands through cross-linking, I can track changes in mechanical properties. These macroscopic changes are then connected to microscopic changes in

ligand configuration and interaction through comparison with molecular dynamics simulations. A final Chapter 7 contains brief concluding remarks and an outlook on possible future directions this work has opened up. This is followed by Appendices on the nanoparticle synthesis recipes.

1.1 References

1. Shevchenko, E. V.; Talapin, D. V.; Kotov, N. A.; O'Brien, S. & Murray, C. B. Structural diversity in binary nanoparticle superlattices. *Nature*, **439**, 55-59 (2006).

2. Dong, A.; Chen, J.; Vora, P. M.; Kikkawa, J. M. & Murray, C. B. Binary nanocrystal superlattice membranes self-assembled at the liquid-air interface. *Nature*, **466**, 474-477 (2010).

3. Cheng, W. L.; Campolongo, M. J.; Cha, J. J.; Tan, S. J.; Umbach, C. C.; Muller, D. A. & Luo, D. Free-standing nanoparticle superlattice sheets controlled by DNA. *Nat. Mater.*, **8**, 519-525 (2009).

4. Cheng, W. L.; Campolongo, M. J.; Cha, J. J.; Tan, S. J.; Umbach, C. C.; Muller, D. A. & Luo, D. Freestanding ultrathin nano-membranes via self-assembly. *Nano Today*, **4**, 482-493 (2009).

5. Liao, J.; Zhou, Y.; Huang, C.; Wang, Y. & Peng, L. Fabrication, transfer, and transport properties of monolayered freestanding nanoparticle sheets. *Small*, **7**, 583-587 (2011).

6. Panthani, M. G. & Korgel, B. A. Nanocrystals for electronics. *Annu. Rev. Chem. Biomol. Eng.*, **3**, 287-311 (2012).

7. Van Rijn, P.; Tutus, M.; Kathrein, C.; Zhu, L. L.; Wessling, M.; Schwaneberg, U. & Boker, A. Challenges and advances in the field of self-assembled membranes. *Chem. Soc. Rev.*, **42**, 6578-6592 (2013).

8. Yan, C.; Arfaoui, I.; Goubet, N. & Pileni, M.-P. Soft supracrystals of Au nanocrystals with tunable mechanical properties. *Adv. Funct. Mater.*, **23**, 2315-2321 (2013).

9. Gauvin, M.; Wan, Y.; Arfaoui, I. & Pileni, M.-P. Mechanical properties of Au supracrystals tuned by flexible ligand interactions. *J. Phys. Chem. C.,* **118**, 5005-5012 (2014).

10. Jeong, Y.; Chen, Y.-C.; TUrksoy, M. K.; Rana, S.; Tonga, G. Y.; Creran, B.; Sanyal, A.; Crosby, A. J. & Rotello, V. M. Tunable elastic modulus of nanoparticle monolayer films by host-guest chemistry. *Adv. Mater.*, **26**, 5056-5061 (2014).

11. Lane, J.M.D. & Grest, G.S. Assembly of responsive-shaped coated nanoparticles at water interfaces. *Nanoscale*, **6**, 5132-5137 (2014).

12. Min, Y.; Akbulut, M.; Kristiansen, K.; Golan, Y. & Israelachvili, J. The role of interparticle and external forces in nanoparticle assembly. *Nat. Mater.*, **7**, 527 (2008).

13. Nie, X.; Petukhova, A. & Eumacheva, E. Properties of emerging applications of self-assembled structures made from inorganic nanoparticles. *Nat. Nanotechnol.*, **5**, 15 (2010).
14. Geim, A. K. & Novoselov, K. S. The rise of graphene. *Nat. Mater.*, **6**, 183-191 (2007).

15. Bishop, K.J.M.; Wilmer, C. E.; Soh, S. & Grzybowski, B.A. Nanoscale forces and their uses in self-assembly. *Small*, **5**, 1600-1630 (2009).

16. He, J.; Lin, X. M.; Chan, H.; Vukovic, L. Kral, P. & Jaeger, H.M. Diffusion and filtration properties of self-assembled gold nanocrystal membranes. *Nano Lett.*, **11**, 2430-2435 (2011).

17. Kanjanaboos, P.; Lin, X.M.; Sader, J.E.; Rupich, S.M.; Jaeger, H. M. & Guest, J. R. Self-assembled nanoparticle drumhead resonators. *Nano Lett.*, **11**, 2430-2435 (2013).

18. Talapin, D.V. & Murray, C. B. PbSe nanocrystal solids for n- and p- channel thin film field-effect transistors. *Science*, **310**, 86-89 (2005).

19. Griffith, A. A. The phenomena of rupture and flow in solids. *Trans. R. Soc. London, Ser. A*, **221**, 163 (1921).

20. Thomson, R. M. J. Physics of fracture. *Phys. Chem. Solids.*, **48**, 965-983 (1987).

21. Hutchinson, J. W. & Suo, Z. Mixed mode cracking in layered materials. *Adv. Appl. Mech.,* **29**, 63 (1991).

22. Fineberg, J. & Marder, M. Instability in dynamic fracture. *Phys. Rep.,* **313**, 1-108 (1999).

23. Bouchbinder, E.; Fineberg, J. & Marder, M. Dynamics of simple cracks. *Annu. Rev. Condens. Matter Phys*., **1**, 371-395 (2010).

24. Long, R.; Hui, C.-Y; Cheng, W.; Campolongo, M. & Luo, D. Size effect on failure of pre-stretched free-standing nanomembranes. *Nanoscale Res. Lett.*, **5**, 1236-1239 (2010).

25. Cox, B. N., Gao, H.; Gross, D. & Rittel, D. Modern topics and challenges in dynamic fracture. *J. Mech. Phys. Solids*, **53**, 565-596 (2005).

26. Jiang, Z.; He, J.; Deshmukh, S. A.; Kanjanaboos, P.; Kammath, G.; Wang, Y.; Sankaranarayanan, S. R. S.; Wang, J.; Jaeger, H. M. & Lin, X. M. Subnanometre ligand-shell asymmetry leads to Janus-like nanoparticle membranes. *Nat. Mater.*, **14**, 912-917 (2015).

27. Kanjanaboos, P.; Joshi-Imre, A.; Lin, X. M. & Jaeger, H. M. Strain patterning and direct measurement of Poisson's ratio in nanoparticle monolayer sheets. *Nano Lett.,* **11**, 2567-2571 (2011).

28. Zharnikov, M. & Grunze, M. Modification of thiol-derived self-assembling monolayers by electron and x-ray irradiation: scientific and lithographic aspects. *J. Vac. Sci. Technol., B: Microelectron. Nanometer Struct. –Process., Meas., Phenom.*, **20**, 1793-1807 (2001).

29. Zhou, C.; Trionfi, A., Hsu, J. W. P. & Walker, A. V. Electron-beam-induced damage of alkanethiolate self-assembled monolayers (SAMS): dependence on monolayer structure and substrate conductivity. *J. Phys. Chem. C.*, **114**, 9362-9369 (2010).

30. Mueggenburg, K. E.; Lin, X. M.; Goldsmith, R. H.; Jaeger, H. M. Elastic membranes of close-packed nanoparticle arrays. *Nat. Mater.* **6**, 656-660 (2007).

31. He, J.; Kanjanaboos, P.; Frazer, N. L.; Weis, A.; Lin, X. M. & Jaeger, H. M. Fabrication and mechanical properties of large-scale freestanding nanoparticle membranes. *Small*, **6**, 1449-1456 (2010).

32. Landman, U. & Luedtke, W. D. Small is different: energetic, structural, thermal, and mechanical properties of passivated nanocluster assemblies. *Faraday Discuss.,* **125**, 1-22 (2004).

CHAPTER 2

NANOPARTICLE SYNTHESIS AND SELF-ASSEMBLY METHODS

2.1 Nanoparticle synthesis

In our experiments, Au nanoparticles with ~5.2 nm core diameter were synthesized using a digestive ripening method.[1,2] The synthesis was a single-phase reaction in a cationic surfactant solution. The prepared nanoparticles were then coated by dodecanethiol through ligand exchange, followed by extensive washing with ethanol and finally dissolving in toluene. A digestive ripening process was adopted in an environment of excess thiol, which can greatly narrow the particle size distribution.

Au nanoparticles with ~9.1 nm core diameter were synthesized with citrate reduction in water and subsequently transferred into organic solvents.[3] In all cases, the Au nanoparticle cores were stabilized with dodecanethiol ligands. The particles were kept as concentrated solutions, suspended either in toluene or chloroform. Here I describe the recipes for these two synthesis methods. Details of these two methods can be found in Appendix A.

After synthesis, the diameters of these nanoparticles were measured by transmission electron microscopy (TEM). The size distribution of these nanoparticles was found to be 5.2 ± 0.3nm for the smaller particles and 9.1 ± 0.5nm for the larger particles, around 5% of the diameter. This

narrow size distribution contributes to the large size (~μm) of well-ordered, nearly close-packed particle arrangements within the self-assembled nanoparticle membranes.

2.2 Nanoparticle self-assembly

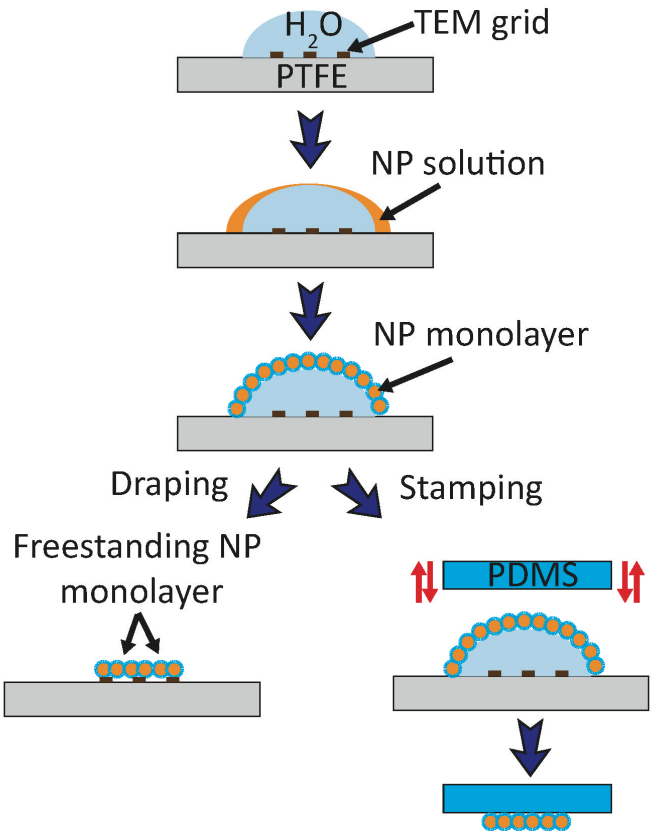

Figure 2.1 Sketch of nanoparticle monolayer self-assembly on an air–water interface and the formation of a freestanding monolayer on a TEM grid after water has evaporated. Two fabrication methods, called draping and stamping, are indicated.

In this thesis, I used an interfacial self-assembly technique to assemble the synthesized nanoparticles into monolayers.[4-9] To assemble a nanoparticle monolayer, 30μl of the concentrated nanoparticle solution was deposited around the perimeter of a 300μl distilled water drop (>18 MΩ) on a flat Teflon surface. The nanoparticles climb quickly to the top of the water

drop and form a close-packed monolayer at the water-air interface (Figure 2.1). The monolayer can then be transferred to different substrates either by letting the water evaporate so the layer drapes itself onto a substrate pre-immersed inside the water drop, or by stamping the particles directly off the water-air interface by touching it with a substrate (Figure 2.1). A variation of the draping technique situates the water drop not on a flat surface but inside a cone shaped support, with the substrate at the bottom (details are discussed in Chapters 4&5).

To transfer nanoparticle membranes onto other substrates more efficiently, I developed a soft-printing technique using a polydimethylsiloxane (PDMS) stamp die. PDMS is a soft silicon-based organic polymer with Young's modulus of several MPa. By gently pushing the PDMS onto the water-air interface covered with nanoparticles, the nanoparticle membrane can be picked up by clinging to the PDMS surface. The PDMS surface with the nanoparticle membrane can then be pushed gently against other substrates (i.e. SiO_2 or SiN), and the membrane was found to easily attach to these other substrates without being damaged. We believe this is due to the surface adhesion energy being lower between nanoparticle membrane and PDMS than with substrates like SiO_2 and SiN. Note that the nanoparticles tend to sinter faster on PDMS surfaces, so this stamping process needs to be completed fast, usually within several minutes.

As also shown in Figure 2.1, freestanding monolayers can be fabricated by simply letting a nanoparticle monolayer that self-assembled at the air-water interface drape itself over a substrate. In this specific case the substrate was a carbon-coated TEM grid with a prefabricated array of 2μm diameter holes. As the water evaporated, the nanoparticle monolayer draped itself onto the substrate and could span across these holes. The inset to Figure 1.1 shows how freestanding

monolayers can maintain good local order. The membranes were found to have very high coverage on these 2μm diameter holes. However, as the hole diameter becomes larger, the coverage of freestanding membranes becomes less efficient, and the largest hole sizes membranes made from 5.2nm Au nanoparticles could cover was found to be $7\ to\ 10\mu m$.

To assemble nanoparticle multilayers, we used a layer-by-layer deposition process in which we applied the stamping technique several times to transfer nanoparticle monolayers from the drop surface to the substrate. The number of layers assembled in this case is simply the number of stamping processes applied. The nanoparticle multilayers prepared by this method are randomly packed between different layers, thus do not have any registration among layers along the thickness dimension.

2.3 Nanoparticle characterization techniques

The nanoparticles used in this thesis all have diameters of $< 10nm$. In order to resolve individual nanoparticles and the local packing structure of the self-assembled layers, electron microscopy is the most straightforward technique. Scanning Electron Microscopy (SEM) is commonly used to image nanoparticles on (semi-) conductive substrates such as $Si/SiO_2/SiN$ (Figure 1.1, Figure 2.2a, *etc*). However, if the substrate is non-conductive, SEM imaging can cause severe charging effects and special techniques such as beam deceleration or electron neutralization need to be used to improve the image quality.

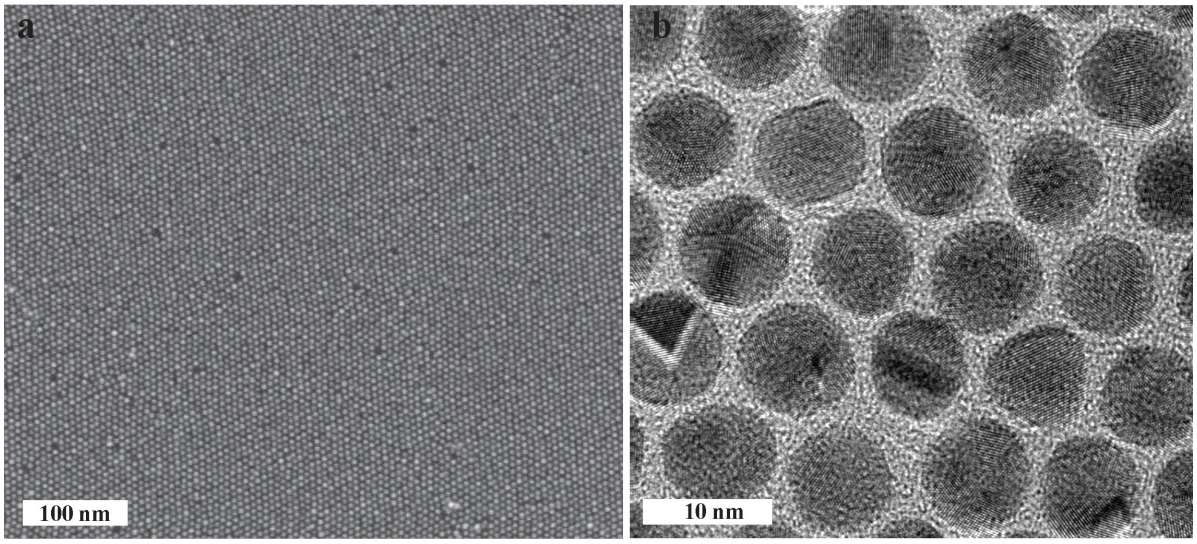

Figure 2.2 (**a**) SEM image of a ~5.2nm Au nanoparticle deposited on SiO_2 substrate. The nanoparticle packing and defects can be clearly seen in this image. (**b**) TEM image of ~9.1nm Au nanoparticles suspended on a TEM grid. The size and shape of nanoparticles can be easily seen from this image, and the crystalline packing of Au atoms inside these nanoparticles can also be resolved. Color variations in the TEM image results from different Au atom packing orientations.

The image resolution from SEM, however, is not high enough to identify the nanoparticle shape or give an accurate measurement of the nanoparticle sizes. To achieve higher imaging resolution, Transmission Electron Microscope (TEM) is used (Figure 2.2b). However, one limitation for TEM comes from its requirement for special sample preparation. In TEM a beam of electrons is transmitted through the sample, thus the sample needs to be ultrathin (typically $< 100nm$). In prior work in our lab, we therefore used special "window" substrates that were TEM transparent.[4,5] In this thesis commercially made TEM grids (copper or carbon coated) with nanoparticle membranes draped or stamped are usually used.

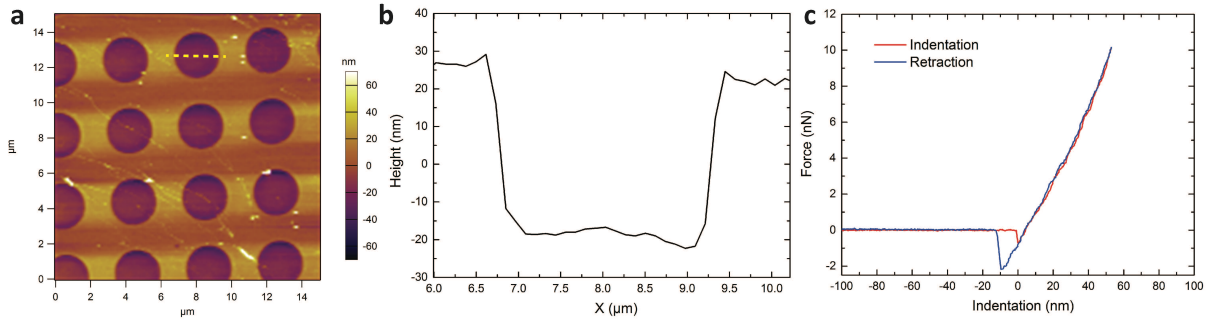

Figure 2.3 (a) Atomic force microscopy (AFM) tapping mode image of Au nanoparticle monolayer draped onto a carbon coated TEM grid with 2μm diameter holes. The image represents height profiles of the sample and dark circular regions are freestanding membranes across the holes. **(b)** Cross section height profile of one of the freestanding membranes shown by yellow dashed line in **(a)**. The freestanding membrane recedes from the edge of the hole by ~50nm due to van der Waals adhesion with the wall, and the height fluctuation in the freestanding area is less than 5nm. **(c)** Example of a typical force-indentation curve, taken at the center of freestanding areas as shown in **(a).** The red curve shows indentation of the probe, while the blue curve represents retraction. During both indentation and retraction, the probe has a sudden jump when engaging or leaving the membrane, due to van der Waals attraction between the probe and the membrane. Little hysteresis was found during the indentation and retraction data, indicating insignificant plastic deformation in the membrane during indentation.

Besides imaging the morphology of the nanoparticle membranes, another important aspect is to study the membranes' response to mechanical perturbations. Atomic force microscope (AFM) imaging and indentation are used for this purpose. Tapping mode AFM imaging, in which the cantilever is driven to oscillate up and down at or near its resonance frequency while scanning over the sample, can be used to obtain the height profile of the sample. With static AFM indentation the AFM cantilever is controlled to apply a specified force ($nN\ to\ \mu N$range) to the sample and measure the resulting sample displacement. Figure 2.3 shows a typical AFM tapping mode scanning image of a sample containing an array of nanoparticle membranes and also shows examples of the force-indentation curves. These indentation data can be combined with elastic theory to obtain the membrane's mechanical properties such as pre-stress and Young's modulus.

To extract the membranes' intrinsic mechanical properties from such force curves, we used a previously developed linear model for a thin elastic disk clamped along the circumference that is subjected to center loading. The force response F and indentation depth δ can be related by:[4,5,10]

$$F = \sigma^{2D}\pi\delta + E^{2D}(q^3 R)(\frac{\delta}{R})^3 \quad (2.1)$$

Here σ^{2D} is the pre-stress in the membrane coming from both the fabrication process and clamping at the wall; R is the radius of the membrane; q is a constant depending on the Poisson ratio ν (q=1.02 in our case where $\nu = 0.34$); E^{2D} is the 2D Young's modulus of the membrane, which is related to the 3D Young's modulus E by $E^{2D} = E \cdot t$, where t is the physical membrane thickness including the diameter of the nanoparticle core and the thickness of the ligand shell. Using this clamped-disk model, we can fit the experimental force-indentation curves to Equation 2.1 and obtain the fitting parameters σ^{2D} and E. This linear model works well as long as δ/R <<1,[5,10] which is easily satisfied for the membranes investigated in this thesis, where $\delta \lesssim 50\text{nm}$ and typical hole diameters are 2R > 1μm.

2.4 References

1. Lin, X. M.; Sorensen, C. M. & Klabunde, K. J. Digestive ripening, nanophase segregation and superlattice formation in gold nanocrystal colloids. *J. Nanoparticle. Res.* **2**, 157 (2000).

2. Lin, X. M.; Jaeger, H. M.; Sorensen, C. M. & Klabunde, K. J. Formation of long-range-ordered nanocrystal superlattices on silicon nitride substrates. *J. Phys. Chem. B,* **105**, 3353-3357 (2001).

3. Liao, J.; Bernard, L.; Langer, M.; Schonenberger, C. & Calame, M. Reversible formation of molecular junctions in 2D nanoparticle arrays. *Adv. Mater.* **18**, 2444 (2006).

4. Mueggenburg, K. E.; Lin, X. M.; Goldsmith, R. H.; Jaeger, H. M. Elastic membranes of close-packed nanoparticle arrays. *Nat. Mater.* **6**, 656-660 (2007).

5. He, J.; Kanjanaboos, P.; Frazer, N. L.; Weis, A.; Lin, X. M. & Jaeger, H. M. Fabrication and mechanical properties of large-scale freestanding nanoparticle membranes. *Small*, **6**, 1449-1456 (2010).

6. Kanjanaboos, P.; Lin, X.M.; Sader, J.E.; Rupich, S.M.; Jaeger, H. M. & Guest, J. R. Self-assembled nanoparticle drumhead resonators. *Nano Lett*., **11**, 2430-2435 (2013).

7. Wang, Y.; Kanjanaboos, P.; Barry, E.; Mcbride, S.; Lin, X. M. & Jaeger, H. M. Fracture and failure of nanoparticle monolayers and multilayers. *Nano Lett.*, **14**(2), 826-830 (2014).

8. Wang, Y.; Kanjanaboos, P.; McBride, S. P.; Barry, E.; Lin, X. M. & Jaeger, H. M. Mechanical properties of self-assembled nanoparticle membranes: stretching and bending. *Faraday Discuss.* **181**, 325-338 (2015).

9. Wang, Y.; Liao, J.; McBride, S. P.; Efrati, E. Lin, X. M. & Jaeger, H. M. Strong resistance to bending observed for nanoparticle membranes. *Nano Lett.*, **15**, 6732-6737 (2015).

10. Lee, C.; Wei, X.; Kysar, J. W. & Hone, J. Measurement of the elastic properties and intrinsic strength of monolayer graphene. Science **321**, 385-388 (2008).

CHAPTER 3

FRACTURE AND FAILURE OF SELF-ASSEMBLED NANOPARTICLE MEMBRANES*

3.1 Introduction

In nanoparticle-based solids, metallic or semiconducting particles, separated by short molecular linkers or ligands, play the role of "designer atoms" that can organize into superlattice configurations.[1-4] However, for these systems one of the key questions in materials science has remained largely unanswered, namely when and how failure under applied stress loading occurs.[5-9]

Here, we address this for failure under tensile load and focus on the ultrathin film limit in which the thickness approaches that of a single layer of nanoparticles. In this limit, technologically relevant for flexible coatings and self-assembled electronic components, uniform monolayers of close-packed particles with few major defects prior to applying any strain can be fabricated and multilayered structures can be assembled with precision by successively depositing layers one at a time. Given the hybrid organic–inorganic nature of nanoparticle films, intriguing issues include to what extent the linkers can withstand stresses before rupturing and how the fracture patterns differ from those of ultrathin coatings of pure inorganic material. A special feature of nanoparticle monolayers is that, unlike in atomic systems, fracture patterns can be imaged with relative ease down to individual constituent particles using scanning and transmission electron

* This Chapter is largely based on Wang, Y.; Kanjanaboos, P.; Barry, E.; Mcbride, S.; Lin, X. M. & Jaeger, H. M. Fracture and failure of nanoparticle monolayers and multilayers. *Nano Lett.*, **14**(2), 826-830 (2014).

microscopy (SEM and TEM). Statistical analysis of the distribution of crack fragment widths then provides estimates of the intrinsic fracture strength set by the ligand-mediated interparticle bonds.

3.2 Experiment setup

In our experiments, the nanoparticles consist of gold cores stabilized by dodecanethiol ligands in either toluene or chloroform. Particles with core diameters of 5.2 ± 0.3 nm were synthesized using digestive ripening techniques,[10,11] and particles of 9.1 ± 0.5 nm in diameter were synthesized through citrate reduction in water and subsequently transferred into organic solvents.[12] Nanoparticles were assembled at an air–water interface by adding 30 μL of a concentrated solution to droplets of 18.2 MΩ distilled water (300 μL).[13-16] Under these conditions, drying-mediated self-assembly results in close-packed monolayers that are mechanically robust and have Young's moduli E_f on the order of ~5 GPa.[13,14] The monolayers were transferred onto polydimethylsiloxane (PDMS) substrates (6.0 cm × 1.5 cm × 5 mm) by gently placing the substrate into contact with a monolayer. The PDMS substrates were made by mixing the base and curing agent (SYLGARD 184 Silicone Elastomer Kit, Fisher Scientific) with a ratio of 7:1, followed by degassing and curing at 70 °C for an hour. Atomic force microscopy (AFM) characterization of the PDMS gave a Young's modulus $E_s \approx 2.9$ MPa and a rms roughness of <1 nm (measured over 400 μm^2 as well as 1 μm^2 areas). With the monolayer attached, the elastomer substrate was stretched in an Instron 5869 materials tester (Figures 3.1&3.2). A strain rate of ~0.01 s^{-1} was used to ensure that the process was quasi-static. At this strain rate, the viscous modulus of our PDMS material, measured directly with a rheometer

(MCR 301, Anton Paar), was 0.03 MPa; since this is only about 1% of E_s, viscous effects from the substrate can thus be neglected. Once in their strained state, the Au nanoparticle monolayers were removed from the PDMS and fixed to a solid surface by pressing a clean piece of silicon against them. A FEI Nova NanoLab SEM was used to image the crack pattern. For the data discussed below, 3 independent samples at each strain level were investigated and for each sample over 20 SEM images, taken at random locations, were analyzed. For the remainder of this discussion, the term "fracture" refers only to fracture of monolayers and multilayers, because fracture of the substrate did not occur for the strain levels applied.

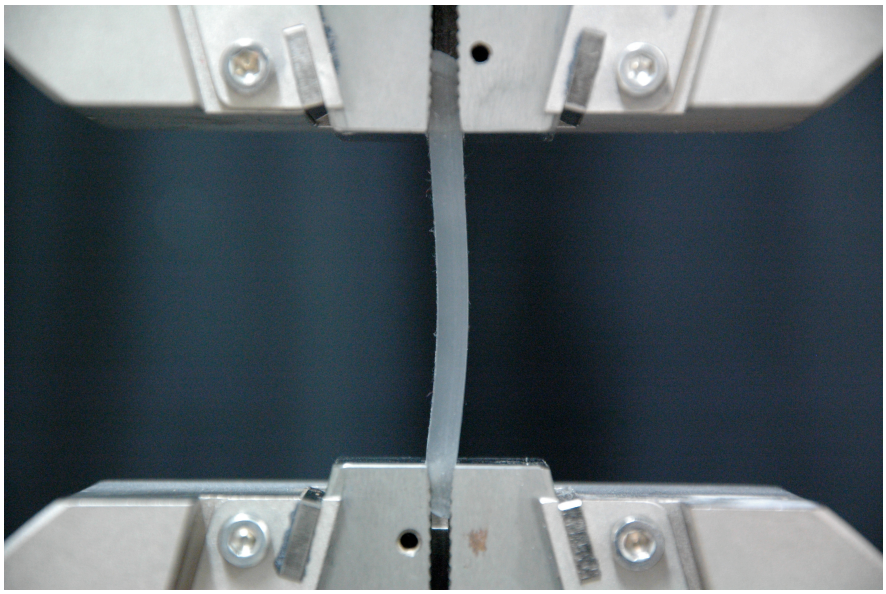

Figure 3.1 Side view of the PDMS substrate initially loaded to the Instron 5869 materials tester. The small curvature of the substrate comes from the clamping from the two grippers, which squeezes more material to the center.

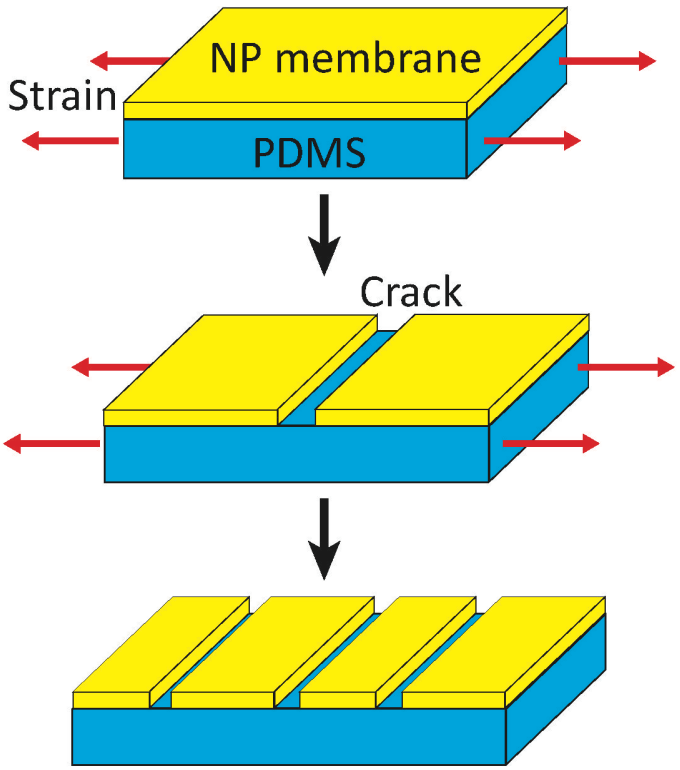

Figure 3.2, Sketch of nanoparticle membranes deposited onto PDMS substrates, showing crack formation under an applied tensile strain.

3.3 Results and Discussion

Representative images of the observed crack patterns are shown in Figure 3.3 a-d. We note that the as-deposited monolayers in our experiments were highly uniform on scales beyond a few tens of particles, and at smaller scales (a few particles across) they consisted of close-packed particle arrangements that formed local, polycrystalline regions separated by grain boundaries. For <5% strain, a few channel cracks appear, mainly at large scale residual deposition defects or occasional multiparticle voids in the film. These are a few micrometers apart and act as nucleation sites for the initial cracks, thus setting the largest crack distance in our experiments.

Increasing the strain to 15% adds straight, but short cracks (<3 μm in length) that run perpendicular to the (horizontal) loading direction. As a result, the monolayer becomes divided into fragments with widths ranging from 200 nm to 1 μm. The fragmentation process continues with strains >15%, however, instead of following straight lines, the new cracks form zigzag shapes, as also observed in related experimental systems.[17]

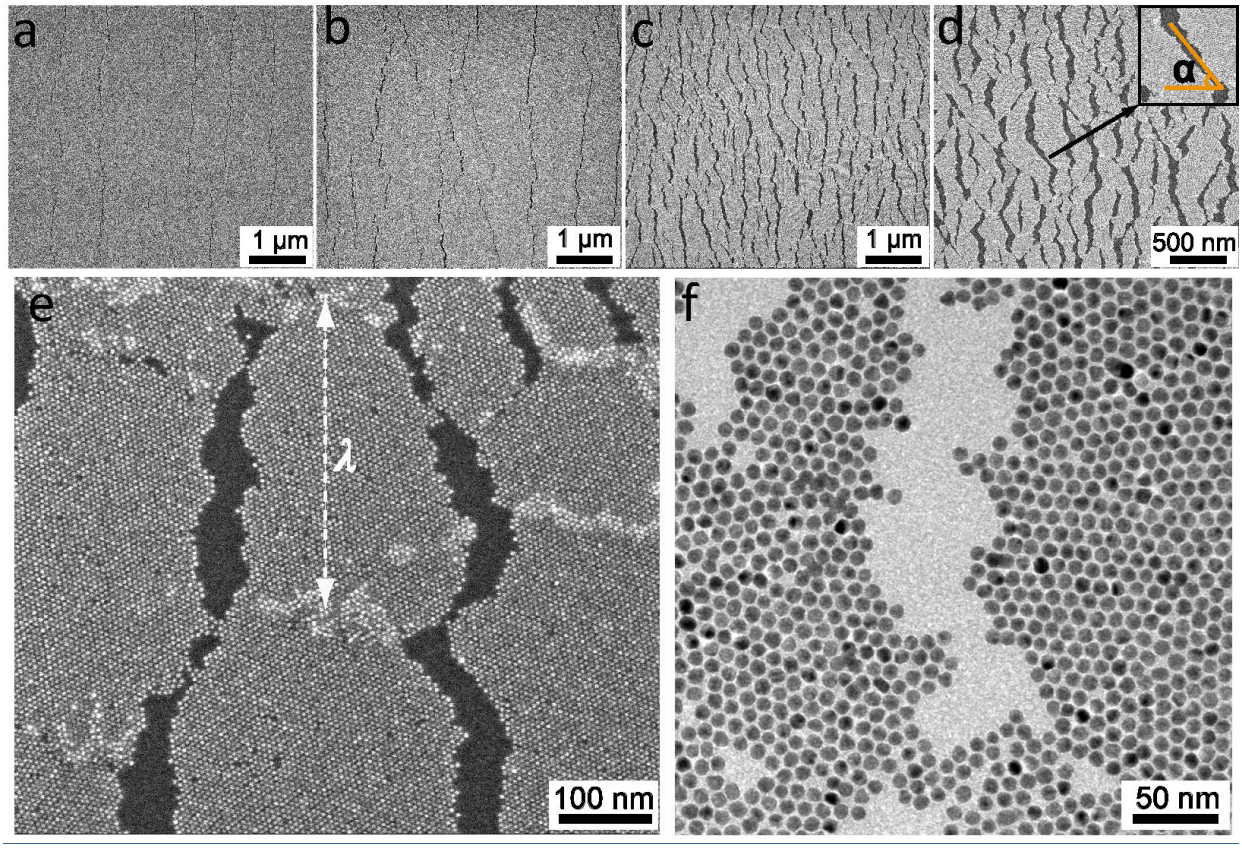

Figure 3.3 (**a–d**) Scanning electron microscope (SEM) images of monolayers of 5.2 nm diameter nanoparticles after applying 5, 8, 30, and 60% strain (left to right). Inset to (d) shows zoomed-in image of a crack and definition of crack angle α. (**e**) Higher-magnification detail of monolayer (c) under 30% strain, dashed line shows wavelength of white strips. (**f**) Transmission electron microscope (TEM) detail of a 9.1 nm diameter nanoparticle monolayer under 20% strain. In all images (a–f), the loading direction is horizontal.

Higher-resolution images indicate that crack edges do not necessarily follow the local lattice orientation of the monolayer (Figure 3.3e). A representative distribution of the angle α between cracks and loading direction is plotted in the inset to Figure 3.4 for different strains. For this plot, α was measured from midlines of crack segments that are longer than 100 nm, and therefore averages over any local, particle-scale roughness along a crack edge (see Figure 3.3d). At low strains (<15%), α has a sharp peak at 90°, as expected. With further strain, more and more cracks tend to form at $\alpha \approx 60°$ rather than 90°. The crossover between these two different crack regimes takes place between 15 and 20% strain. The fact that cracks no longer remain perpendicular to the stress loading direction can be explained by surface instabilities. From bifurcation analysis,[17,18] the preferred value of α at high strains is related to the hardening exponent N in the stress response, $\sigma = K\varepsilon^N$ and varies from 43° ($N \approx 0$) to 61° ($N = 1$). In our experiments, the second peak in α is centered at 60° ± 1°. This provides evidence that the nanoparticle sheets behave like a linearly elastic material with $N \approx 1$. Interestingly, this linear behavior here holds until fracture, and not only for the small perturbations applied in prior work on freestanding nanoparticle films.[13,14,19]

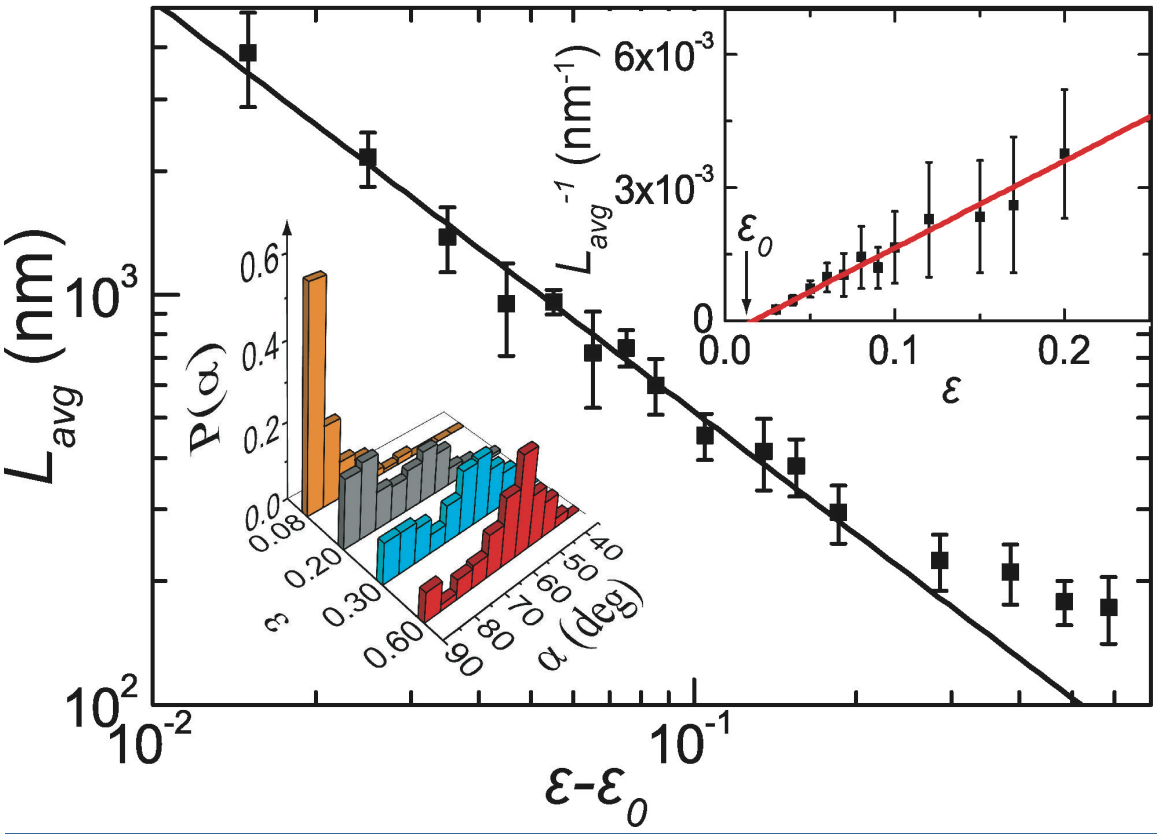

Figure 3.4: Average crack spacing L_{avg} as function of strain $\varepsilon - \varepsilon_0$ for 5.2 nm diameter Au nanoparticle monolayers. Insets: Determination of strain onset ε_0 (upper right); probability distribution $P(\alpha)$ of crack angle α for different strain ε (lower left).

Another characteristic feature of the SEM images in Figure 3.3 are bright, narrow strips along the loading direction, indicating local regions of multilayer formation. These are caused by compression perpendicular to the loading direction[20,21] as the PDMS elastomer is stretched (the Poisson ratios of the monolayer and the PDMS substrate are 0.32 ± 0.02[19] and 0.5, respectively). The thickness of these regions, measured by AFM, is approximately twice that of the monolayer, suggesting that under compression, the monolayer fragments did not buckle or fold into the third dimension (as this would lead to thicknesses of 3 particles or more). Instead, it appears that they broke open locally and started to slide over each other like miniature tectonic plates.

The average wavelength λ_{avg} of these horizontal stripe patterns can give a rough estimate of the monolayer's Young modulus via[20] $\bar{E}_f = 3\bar{E}_s[(\lambda_{avg})/(2\pi h_f)]^3$. Here $\bar{E}_f = E_f/(1 - \nu_f^2)$ and $\bar{E}_s = E_s/(1 - \nu_s^2)$ are the plane strain moduli of monolayer film (f) and PDMS substrate (s); ν_f and ν_s are the associated Poisson ratios; h_f is the monolayer thickness. For the 5.2 nm diameter particles, h_f = 6.9 ± 0.5 nm as measured by AFM (which is smaller than adding the Au core diameter (5.2 nm) and the ligand lengths (1.7 nm)[14] on both sides, probably due to compression of ligand layers during the stamping process), and λ_{avg} = 320 ± 30 nm. From these the monolayer's Young modulus is found to be $E_f \sim$ 3.5–6 GPa, consistent with previous AFM measurements.[13,14]

Analyzing the crack spacing more quantitatively, images were first thresholded and then scanned line by line along the loading direction to identify L_{avg}, the average fragment width or distance between cracks (Figure 3.4). The onset strain ε_0 for cracking is determined by the intercept $L_{avg}(\varepsilon_0) \rightarrow +\infty$, as shown in the inset. The resulting value $\varepsilon_0 \approx$ 1.6% includes two contributions: any initial prestrain in the sample ε_{pre} and the critical strain for fracture ε_c.[22,23] When mounting the PDMS substrate in the Instron, the substrate's ends are squeezed and the substrate elongates (Figure 3.1). As a result, the nanoparticle layer attached to the PDMS is under a compressive prestrain, which we estimate as $\varepsilon_{pre} \approx$ 0.7% from measuring the macroscopic curvature of the slightly bent PDMS substrate. It follows that the onset strain for nanoparticle monolayer fracture ε_c is about 0.9% in our samples.

As shown in Figure 3.4, we see two regimes for the behavior of L_{avg} versus $\varepsilon - \varepsilon_0$: an inverse scaling of the average fragment width L_{avg} with strain above fracture onset $\varepsilon - \varepsilon_0$ up to about 20%, followed by a weaker dependence at higher strains. In general, the inverse scaling could be

preceded by an initial, low-strain regime with wider width distribution and larger L_{avg} due to film heterogeneity.[20,22] The fact that we do not observe this is indicative of the high structural uniformity of our layers at scales >10 particle diameters; local disorder in the particle packing occurs at scales well below the fragment size L_{avg}, which remains >100 nm over the whole range of strains applied. In many other materials and thin metal films, strain localization mechanisms such as local thinning and debonding dominate cracking.[17,24] In our case, given the large ratio of crack spacing to monolayer thickness, the critical strain for debonding is much higher than that for cracking. Thus, the Au monolayer can be assumed to be well bonded to the PDMS substrate,[23] at least up to 15–20% strain.

In this situation, the spatial stress profile in the film can be described by a shear-lag model.[20,25-27] Because of the large mismatch of elastic response between the Au monolayer and the PDMS substrate when stretched, two "shear zones" transfer tensile stress to the layer. The length L_s of a shear zone is determined by[20,26] $L_s \approx (2h_f E_f)/E_s)$. In our case, $L_s > 10$ μm is much larger than the average fragment width, the tensile stress reaches its maximum at the fragment center, and the fragment tends to crack at its midpoint when the maximum tensile stress exceeds σ*, the fracture strength of the layer. Each subpiece cracks again when the strain is doubled, so that the average fragment width varies with applied strain according to[20]

$$L_{avg} = \frac{2h_f\sigma^*}{E_s(\varepsilon - \varepsilon_0)}. \qquad (3.1)$$

This relationship well predicts how the average fragment width changes with applied strain (Figure 3.4). The one free parameter, the average fracture strength, is determined from a fit, which gives σ* = 11.0 ± 2.6 MPa. This value is similar to cross-linked thin polymer films.[20] Because the nanoparticles in monolayers are only connected by short ligand interdigitation with

no cross-linking at all, it is remarkable that their fracture strength is comparable to cross-linked polymer films.

For strains larger than 20%, the plots deviate from the prediction of Equation 3.1. It is likely that at this point the yield strength for interfacial shear is reached and the fragments start to slip on the substrate.[23] The slipping interface makes it harder to crack the fragments further, so the fragmentation rate starts to decrease. Another possible reason is connected with the fact that the data in Figure 3.4 flatten off around 100-200nm domain size, which is the typical length scale associated with the well-packed, almost crystalline domains in the samples. These domains can have a higher strength, causing the plots to deviate from prediction. Other possibilities might include out-of-plane curling of the nanoparticle layer at large strain;[28,29] however, the E_f/E_s ratio in our experiments would suggest that any vertical deformation of a fragment due to curling is <2 nm and thus contributes negligibly to the applied strain.

The fact that these cracks do not propagate as in brittle films[8,9] can be attributed to ductility at their crack tips. Indeed, this is the only evidence we find of deviations from linear elastic behavior. It indicates that the material's behavior at the local, few-particle scale can be quite different, and it corroborates what we observed previously[19] with slits cut into freestanding monolayer sheets, namely that the local particle configuration around the tips of the slits can be deformed significantly under stress.[30]

Of course, the fragments do not always break at exactly the midpoint between two existing cracks and there will be a distribution in the fragment widths. On the basis of a weakest link

picture for failure, which considers material defects across a wide range of scales,[22] a Weibull distribution is commonly assumed. In our experiments, we have sufficient resolution to determine this distribution directly and do not have to make assumptions (Figure 3.5a).

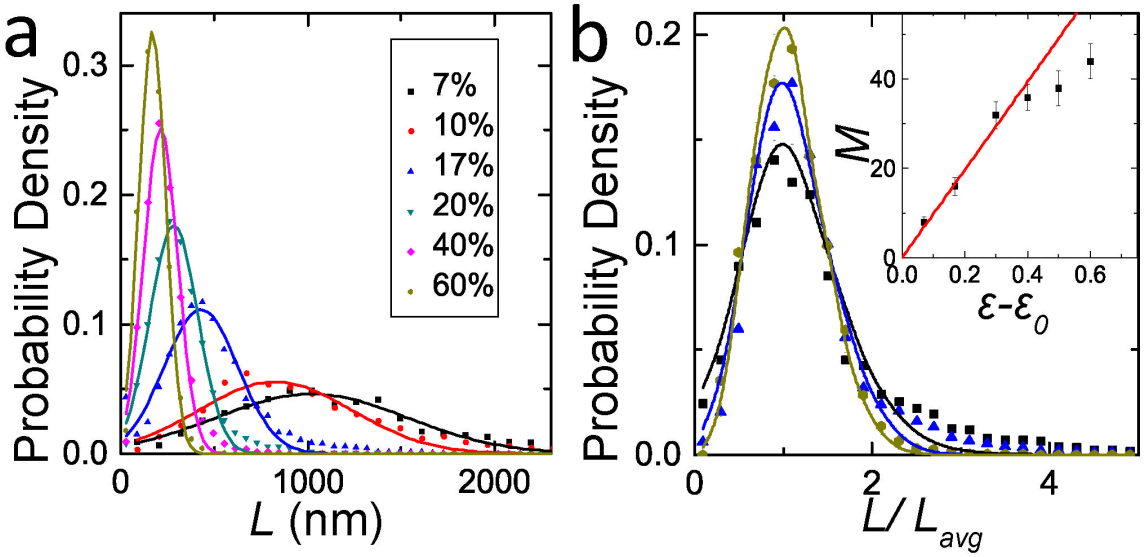

Figure 3.5 (a) Crack spacing distribution for different strains as indicated. Symbols: experimental data; lines: Gaussian fits. (b) Normalized crack spacing distribution. Symbols: experimental data; lines: simulation as described in text. Strain levels are indicated by the same symbols and colors as in (a). Inset: Fitting parameter *M* for different strains.

The fact that a Gaussian distribution fits well points to the absence of macroscopic defects in our samples and suggests that the relevant disorder occurs over a narrow range of length scales.[31] Such a Gaussian fragment width distribution can arise from an interparticle bond strength distribution of Gaussian form. To investigate this, we analyzed a simple one-dimensional (1D) simulation consisting of a chain of particles with fracture strength between neighbors picked from a Gaussian with mean σ* and standard deviation Δσ. The chain is then fragmented by applying the shear-lag model *M* times in succession, and the final fragment widths are analyzed as a function of *M*. Figure 3.5b shows the results using a fixed value of 3.6 MPa chosen to produce the overall best fit to all experimental data (further simulation results

show that deviations from a Gaussian shape, observed in tails of the experimental crack spacing distribution data, might come from the 2D geometry of cracks, both length and orientation, which is not considered in the 1D model). The simulations used an initial chain length of 2000 particles and the data shown are ensemble averaged over 10^4 independent trials. With increasing strain and therefore larger number *M* of fragments, the distribution is found to become narrower, as in the experiments. Furthermore, the variable *M* is seen to be proportional to the experimental strain, at least up to the point that slipping is reached. The considerable width of the fracture strength distribution in the experiments, almost one-third of its mean, can be understood as arising from a combination of factors that all can affect the bond strength, besides local lattice defects also including variations in interparticle spacing or in the ligand coverage of individual particles.

The monolayer strength is a result of the interdigitation of ligands from neighboring particles. The degree of this interdigitation will depend on the curvature of particles, and thereby the particle size[14]. This suggests that increasing the particle size should increase fracture strength. This is indeed what we find when switching to larger Au cores (9.1 nm diameter) with the same capping ligands (Figure 3.3f). The resulting ~10 nm thick monolayers were found to have a fracture strength of 15.2 ± 1.7 MPa (Figure 3.6), roughly 40% higher than that of the ~6.9 nm thick monolayers.

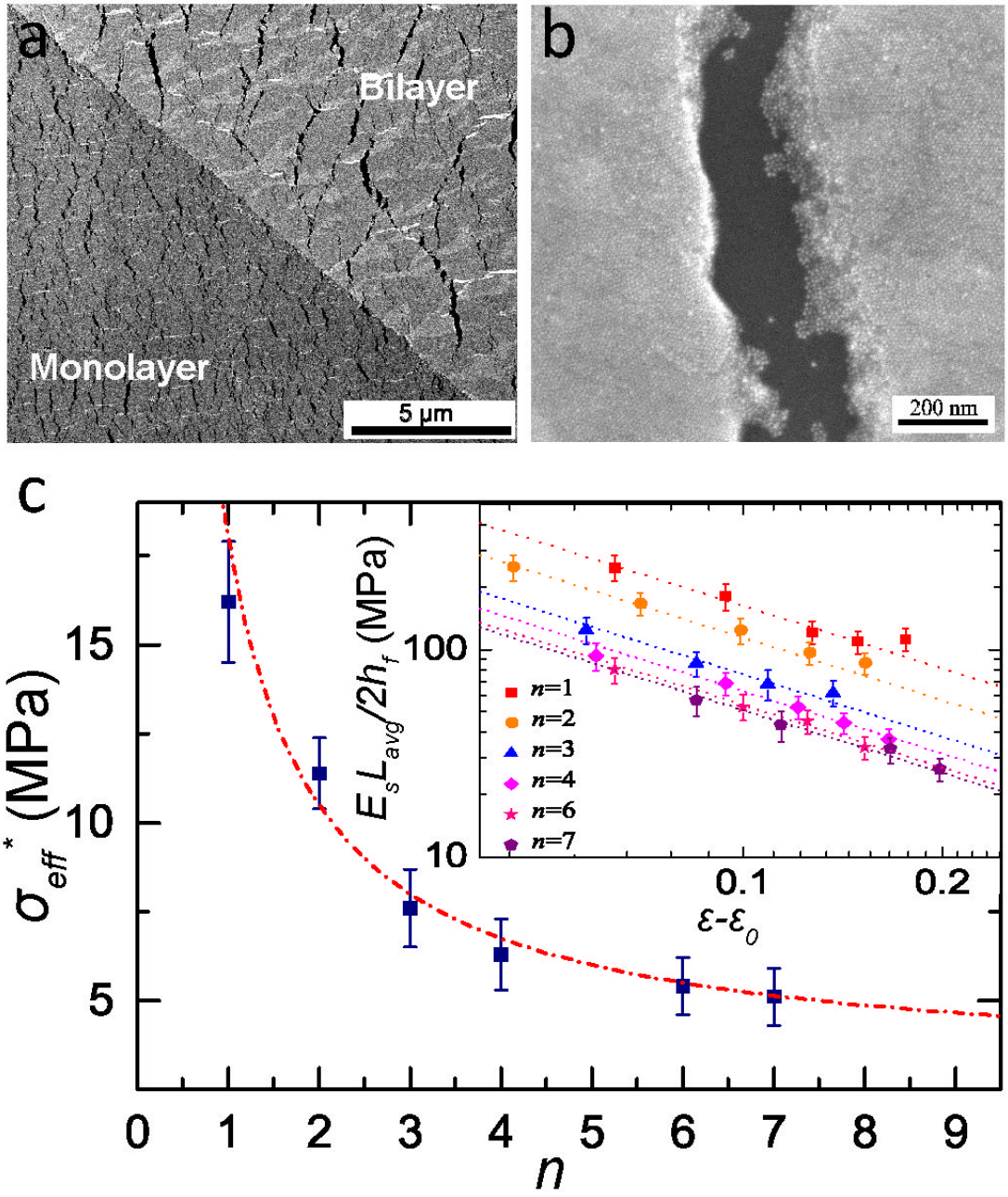

Figure 3.6 (**a**) SEM image of step-edge region with monolayer in the lower left and bilayer in upper right (9.1 nm diameter Au nanoparticles). The second layer was stamped onto the first layer before the underlying PDMS substrate was strained to 20%. (**b**) Zoomed in SEM image of a crack propagated in a 7-layer nanoparticle multilayer after stretching. (**c**) Dependence of effective fracture strength σ_{eff}^* on film thickness, parametrized by number of monolayers n, for 9.1 nm diameter Au nanoparticles. Inset: Normalized average crack spacing $E_s L_{avg}/2h_f$ as function of strain for different n, with dashed lines indicating power law with exponent −1 (Eq. 3.1). The vertical position of the lines in this log–log plot gives the effective fracture strength.

Building up thicker films, a monolayer at a time, our experiments can directly investigate how film thickness affects fracture. In partially overlaid monolayers on the same substrate, where they are subjected to the same applied strain, differences are immediately noticeable when comparing regions on either side of a step-edge. As shown in Figure 3.6a, the crack spacing in the bilayer region is clearly larger than in the monolayer, and cracks tend to stop at the step-edge. Analyzing the average crack spacing L_{avg} for films n = 1 to 7 layers thick (Figure 3.6c inset), we find that Equation 3.1 remains valid but with an effective fracture strength σ_{eff}^* that decreases with increasing n before eventually saturating. Similar behavior is observed in thin metal coatings that have been grown on substrates,[21] where it is typically attributed to larger initial defect sizes in thicker films. However, our system is deposited "layer-by-layer", and the initial defect sizes are not expected to change with the number of layers. Instead, we believe this behavior is indicative of inhomogeneity in stress across the thickness.[32] Because all layers were prepared the same and from the same set of nanoparticles, it is unlikely they varied significantly in inherent strength. However, the first monolayer is deposited on the PDMS substrate and thus likely to exhibit different prestress compared to the subsequent layers. The fact that the effective fracture strength decreases implies that, at fracture, the 2^{nd}–n^{th} layers have taken up proportionally less stress than the first layer; for example, they started out at some residual stress level that was lower than that of the first layer. Once the stress in the first layer exceeds σ^*, the fracture will propagate across the full film thickness $h_f = nh_0$, where h_0 is an individual layer thickness. This point defines σ_{eff}^* for the n-layer system. If we assume the simplest case, where the residual stress in the first layer is larger by a fixed amount $\Delta\sigma_r$, we have $\sigma_{eff}^* = [\sigma^* h_0 + (n - 1)(\sigma^* - \Delta\sigma_r)h_0]/nh_0) = \sigma^* - \Delta\sigma_r + (\Delta\sigma_r/h)$. This matches the data very well with $\Delta\sigma_r = 0.8\sigma^* \approx 12$ MPa (Figure 3.6c red dashed line), implying a residual strain difference $\Delta\varepsilon_r = (\Delta\sigma_r/E_f) \approx 0.3\%$.

3.4 Conclusion

In summary, we investigated microcrack patterns in self-assembled close-packed Au nanoparticle layers. From the fragment width distribution, we extracted the intrinsic fracture strength and its distribution and related it to the interparticle bond strength. Relative to their thickness, monolayers were found to be significantly stronger than multilayers, an effect that we tracked here in detail for the first time and attributed to differences in residual strain during deposition.

3.5 References

1. Shevchenko, E. V.; Talapin, D. V.; Kotov, N. A.; O'Brien, S. & Murray, C. B. Structural diversity in binary nanoparticle superlattices. *Nature*, **439**, 55-59 (2006)

2. Mueggenburg, K. E.; Lin, X. M.; Goldsmith, R. H.; Jaeger, H. M. Elastic membranes of close-packed nanoparticle arrays. *Nat. Mater.* **6**, 656-660 (2007).

3. Cheng, W. L.; Campolongo, M. J.; Cha, J. J.; Tan, S. J.; Umbach, C. C.; Muller, D. A. & Luo, D. Free-standing nanoparticle superlattice sheets controlled by DNA. *Nat. Mater*., **8**, 519-525 (2009).

4. Dong, A.; Chen, J.; Vora, P. M.; Kikkawa, J. M. & Murray, C. B. Binary nanocrystal superlattice membranes self-assembled at the liquid-air interface. *Nature*, **466**, 474-477 (2010).

5. Griffith, A. A. The phenomena of rupture and flow in solids. *Trans. R. Soc. London, Ser. A*, **221**, 163 (1921).

6. Thomson, R. M. J. Physics of fracture. *Phys. Chem. Solids.*, **48**, 965-983 (1987).

7. Hutchinson, J. W. & Suo, Z. Mixed mode cracking in layered materials. *Adv. Appl. Mech.,* **29**, 63 (1991).

8. Fineberg, J. & Marder, M. Instability in dynamic fracture. *Phys. Rep.,* **313**, 1-108 (1999).

9. Bouchbinder, E.; Fineberg, J. & Marder, M. Dynamics of simple cracks. *Annu. Rev. Condens. Matter Phys*., **1**, 371-395 (2010).

10. Lin, X. M.; Sorensen, C. M. & Klabunde, K. J. Digestive ripening, nanophase segregation and superlattice formation in gold nanocrystal colloids. *J. Nanoparticle. Res.* **2**, 157 (2000).

11. Lin, X. M.; Jaeger, H. M.; Sorensen, C. M. & Klabunde, K. J. Formation of long-range-ordered nanocrystal superlattices on silicon nitride substrates. *J. Phys. Chem. B,* **105**, 3353-3357 (2001).

12. Liao, J.; Bernard, L.; Langer, M.; Schonenberger, C. & Calame, M. Reversible formation of molecular junctions in 2D nanoparticle arrays. *Adv. Mater.* **18**, 2444 (2006).

13. Mueggenburg, K. E.; Lin, X. M.; Goldsmith, R. H.; Jaeger, H. M. Elastic membranes of close-packed nanoparticle arrays. *Nat. Mater.* **6**, 656-660 (2007).

14. He, J.; Kanjanaboos, P.; Frazer, N. L.; Weis, A.; Lin, X. M. & Jaeger, H. M. Fabrication and mechanical properties of large-scale freestanding nanoparticle membranes. *Small*, **6**, 1449-1456 (2010).

15. Wang, Y.; Kanjanaboos, P.; Barry, E.; Mcbride, S.; Lin, X. M. & Jaeger, H. M. Fracture and failure of nanoparticle monolayers and multilayers. *Nano Lett.*, **14**(2), 826-830 (2014).

16. Wang, Y.; Kanjanaboos, P.; McBride, S. P.; Barry, E.; Lin, X. M. & Jaeger, H. M. Mechanical properties of self-assembled nanoparticle membranes: stretching and bending. *Faraday Discuss.* **181**, 325-338 (2015).

17. Xiang, Y.; Li, T.; Suo, Z. & Vlassak, J. J. High ductility of a metal film adherent on a polymer substrate. *J. Appl. Phys. Lett.*, **87**, 161910 (2005).

18. Hutchinson, J. W. Surface instabilities on statically strained plastic solids. *Int. J. Mech. Sci.,* **22**, 339-354 (1980).

19. Kanjanaboos, P.; Joshi-Imre, A.; Lin, X. M. & Jaeger, H. M. Strain patterning and direct measurement of Poisson's ratio in nanoparticle monolayer sheets. *Nano Lett.*, **11**, 2567-2571 (2011).

20. Chung, J. Y.; Lee, J.-H.; Beers, K. L. & Stafford, C. M. Stiffness, strength, and ductility of nanoscale thin films and membranes: a combined wrinkling-cracking methodology. *Nano Lett*. **11**, 3361-3365 (2011).

21. Cordill, M. J.; Taylor, A.; Schalko, J. & Dehm, G. Fracture and delamination of chromium thin films on polymer substrates. *Metall. Mater. Trans. A*, **41A**, 870 (2010).

22. Heinrich, M.; Gruber, P.; Orso, S.; Handge, U. A. & Spolenak, R. Dimensional control of brittle nanoplatelets. A statistical analysis of a thin film cracking approach. *Nano Lett.,* **6**, 2026-2030 (2006).

23. Sun, J. Y.; Liu, N. S.; Yoon, J.; Oh, K. H.; Suo, Z. G.; Vlassak, J. J. Debonding and fracture of ceramic islands on polymer substrates. *J. Appl. Phys.*, **111**, 013517 (2012).

24. Stören, S. & Rice, J. R. Localized necking in thin sheets. *J. Mech. Phys. Solids*, **23**, 421-441 (1975).

25. Handge, U. A. Analysis of a shear-lag model with nonlinear elastic stress transfer for sequential cracking of polymer coatings. *J. Mater. Sci.*, **37**, 4775-4782 (2002).

26. Bazhenov, S. L.; Volynskii, A. L.; Alexandrov, V. M.; Bakeev, N. F. Two mechanisms of the fragmentation of thin coatings on rubber substrates. *J. Polym. Sci.*, Part B, **40**, 10-18 (2002).

27. Begley, M. R. & Bart-Smith, H. The electro-mechanical response of highly compliant substrates and thin stiff films with periodic cracks. *Int. J. Solids Struct.*, **42**, 5259-5273 (2005).

28. Douville, N. J.; Li, Z.; Takayama, S. & Thouless, M. D. Fracture of metal coated elastomers. *Soft Matter*, **7**, 6493 (2011).

29. Taylor, A. A.; Cordill, M. J. & Dehm, G. On the limits of the interfacial yield model for fragmentation testing of brittle films on polymer substrates. *Philos. Mag.*, **92**, 3363 (2012).

30. Ritchie, R. O. Mechanisms of fatigue-crack propagation in ductile and brittle solids. *Int. J. Fract.*, **100**, 55 (1999).

31. Lu, C.; Danzer, R. & Fischer, F. D. Fracture statistics of brittle materials: Weibull or normal distribution. *Phys. Rev. E*, **65**, 067102 (2002).

32. Volynskii, A. L.; Panchuk, D. A.; Yarysheva, L. M.; Bazhenov, S. L. & Bakeev, N. F. Structure and properties of the polymer-metal coating interface layer. *Dokl. Phys. Chem.*, **422**, 249 (2008).

CHAPTER 4

FOLDING NANOPARTICLE MEMBRANES INTO 3D STRUCTURES[†]

4.1 Introduction

Folding 2D membranes into 3D structures by directing their internal strain has long been studied in micro- and nano-sized thin films. These folded 3D hollow structures usually have open ends and have wide applications in energy storage and cargo transport. As the thinnest building blocks for nanoparticle based materials, self-assembled nanoparticle membranes have great potential for strain-directed folding, since the elastic properties of the hard particle cores and their soft organic ligands can be tuned independently.

However, most work so far has been limited to treating these membranes as 2D materials. We recently discovered that an asymmetry develops between the two faces of gold-dodecanethiol nanoparticle layers when they are self-assembled at an air-water interface under conditions where the ligand packing density on the particle cores is lower than the maximum.[1] The asymmetry consists of slightly fewer ligands occupying the water-facing side of the monolayer as compared to the air-facing side. In most cases, this asymmetry by itself is not sufficient to drive spontaneous curling up of a membrane toward the side originally facing the water once the

[†]This Chapter is partially based on Wang, Y.; Kanjanaboos, P.; McBride, S. P.; Barry, E.; Lin, X. M. & Jaeger, H. M. Mechanical properties of self-assembled nanoparticle membranes: stretching and bending. *Faraday Discuss.* **181**, 325-338 (2015).

stress is relieved that keeps the membrane tautly stretched across a hole or trench. Indeed, when freestanding membranes have ripped we find portions that spontaneously have bent to either side, likely depending on the precise details of the process that caused the ripping. However, when we use the electron beam from an electron microscope to irradiate a freestanding membrane we induce strain that greatly amplifies the asymmetry.

In this chapter, I describe how we cut freestanding nanoparticle membranes into designed shapes with focused ion beam (FIB), and to demonstrate how e-beam irradiation can be used to bend sections of the membranes in a highly controlled manner toward the originally water-facing side, making it possible to fold membranes and roll them up into 3D structures, for example, hollow nano-scrolls. While this approach offers control, it uses large exposure doses, which makes it slow and furthermore modifies the ligands through a combination of cutting and cross-linking.[2,3]

In order to obtain nanoparticle scrolls in larger quantities and with higher efficiency, we developed another technique where scrolls can be formed spontaneously during the water droplet drying process. This technique utilizes the fact that water only exists at one side of the nanoparticle membrane and swells the ligand layer on that side, which creates a strain gradient and rolls up the membrane. This technique can fabricate nanoparticle scrolls with radii range from ~100nm to ~200nm.

Atomic force microscopy is then used to obtain force and stiffness maps of these structures, which will be further described in the next chapter. The fabrication of hollow nanoparticle scrolls

opens wide applications of nanoparticle based materials in energy storage, drug delivery, and mechanical actuators.

4.2 Experiments and Discussion

Generally, for a flat sheet to bend or curl up spontaneously, there has to be a gradient in strain between its top and bottom face. In our monolayers, such a strain gradient can arise from an asymmetric ligand distribution that develops while the nanoparticles self-assemble at the water–air interface[1]. As mentioned previously, this gradient often is not significant enough to spontaneously produce a large curvature, but it can be amplified very significantly by exposing a freestanding monolayer to an electron beam, for example during SEM or TEM imaging. It is known that electron beams can cause C–H, C–C and C–S bond cleavage, leading to the formation of C=C bonds and cross-links in the monolayer.[2,3] This in turn pulls particles closer together, effectively introducing internal strain.[4] We note that in all these cases, e-beam exposure will bend the monolayer toward the side that originally faced the water. This is the side of the monolayer that exhibits the slightly lower ligand density and therefore can contract slightly more under e-beam exposure, as sketched in Figure 4.1 a1. Since the monolayer is sufficiently thin, the beam will always penetrate fully and it is therefore irrelevant which of the two sides of the layer is facing the e-beam.

To enable this curling process, the membrane has to be able to move and contract. In Figures 4.1 a2-a5 a freestanding nanoparticle monolayer was first cut by a focused ion beam (FIB), producing an "X" shaped slit pattern, and then exposed to successive scans with the SEM

electron beam. Each image is a single full-frame scan at an acceleration voltage of 10 kV and a beam current of ~50 pA. Immediately after the FIB cut and after the first SEM scan the monolayer is still flat, but on increasing the e-beam dose it curls up more and more.

Figure 4.1(b) shows more explicitly how the e-beam exposure exploits the ligand density asymmetry. In this sequence of six SEM scans, a circular monolayer membrane started out partially detached along its perimeter, with a nearly vertical flap that happened to be bent toward the side originally facing away from the water (in the image it faces toward the microscope's secondary electron detector and thus appears bright). Under increasing exposure, the flap is effectively undone by bending it back toward the water-facing side, and then the flap portion continues to roll up into a tight scroll underneath the intact portion of the membrane.

While complicated FIB cut patterns together with an appropriate (and perhaps locally varied) e-beam exposure dose should enable intricate folding patterns, for rolling monolayers into scrolls even a partial rip along the perimeter of the membrane often suffices, as Figure 4.1(b) shows, since it can trigger further ripping as the layer curls up. The most straightforward way to achieve this at high yield without even employing the FIB is to use holes with larger diameters, such as TEM grids with 7.5 μm square holes. Given the longer perimeter, there is a higher probability that a defect or grain boundary resides right at the edge where the freestanding portion of the membrane is tied to the supporting substrate, a spot of high local stress which is thus likely to fail first. Figures 4.1 c&d show how this can quickly produce a variety of scroll shapes under e-beam exposure.

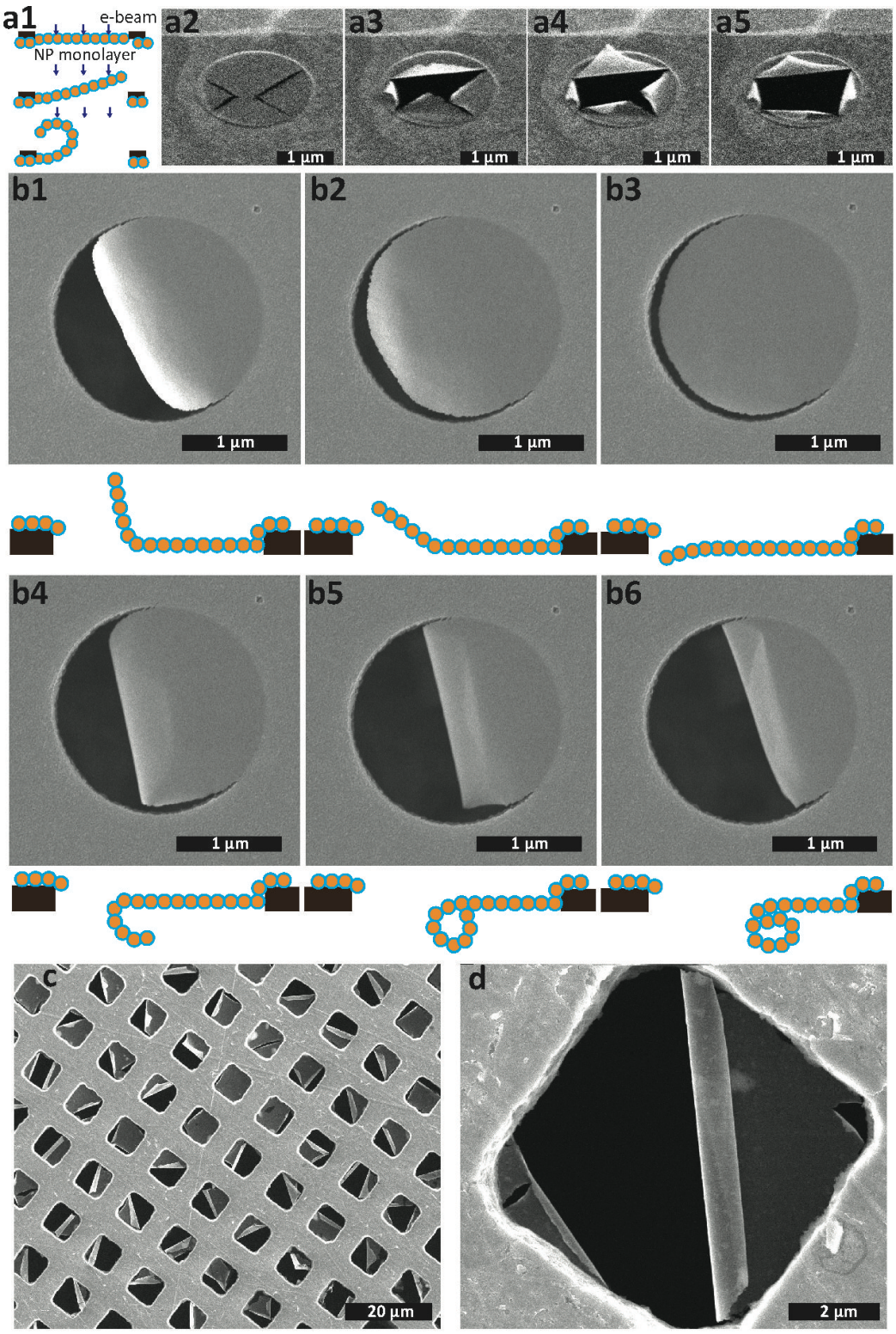

Figure 4.1 (**a1**) Sketch of freestanding monolayer rolling up toward the water-facing side under electron beam irradiation. (**a2–a5**) SEM images of a freestanding monolayer comprised of 5.2 nm Au–dodecanethiol nanoparticles draped over a 2 µm hole in a carbon-coated TEM grid. An X-shaped slit has been cut by a FIB, and the membrane has been exposed to SEM electron beam

scans 1, 8, 15 and 22 times (left to right). (**b1–b6**) Sequence of SEM scans showing the bending and nano-scroll formation of a 5.2 nm Au–dodecanethiol monolayer membrane during e-beam exposure. The sketches underneath the images indicate the process. (**c**) SEM image of the freestanding 5.2 nm Au–dodecanethiol monolayers on a copper TEM grid with 7.5 μm square holes, after exposure to the e-beam for 30 s. (**d**) Zoomed-in image of a nano-scroll from panel (c).

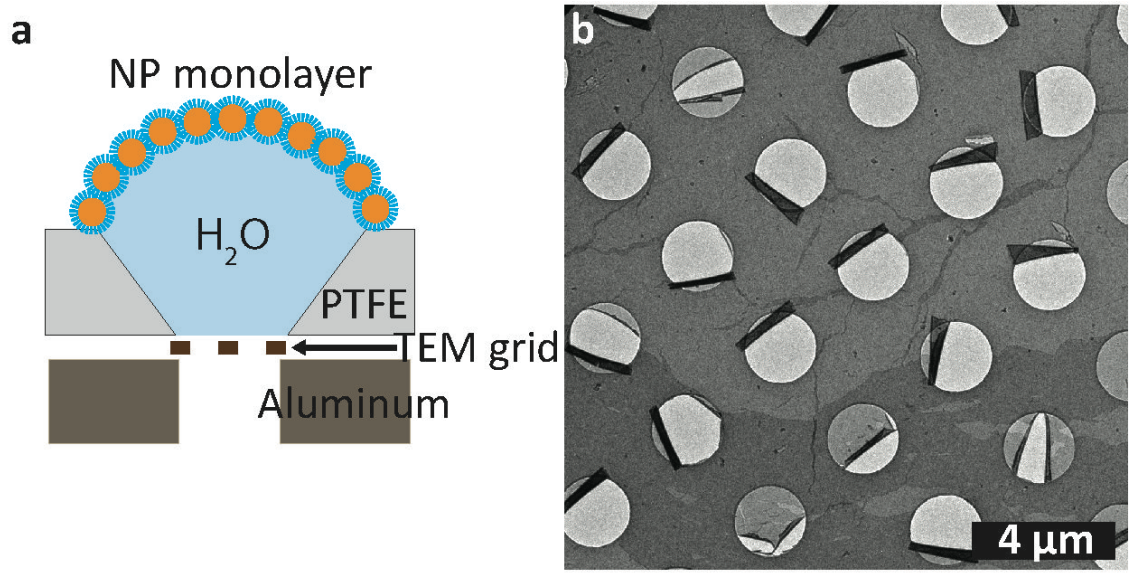

Figure 4.2 (**a**) Schematic of nanoparticle scroll assembly process. (**b**) TEM image of nanoparticle scrolls formed on a carbon-coated TEM grid with 2 μm diameter holes *via* spontaneous self-rolling during the drying process.

Spontaneous drying-induced scroll formation in the absence of e-beam assistance occurred only rarely with appreciable yield, possibly because this requires a rather specific combination of drying condition and ligand concentration in the nanoparticle solution. However, when adjusted properly, it is possible to find large areas in the substrate where arrays of membranes that initially covered holes have detached and self-rolled into nano-scrolls. Figures 4.2 a&b shows results from one such experiment. Here the water droplet with the nanoparticle monolayer at its top interface was contained inside a cone-shaped support fabricated from PTFE. The substrate, a carbon-coated TEM grid (Quantifoil 657-200-CU) containing a regular array of 2 μm diameter holes, was clamped between the PTFE holder and its aluminum counterpart (Figure 4.2a). The nano-scrolls obtained from this technique have an average radius of ~150nm and can be later

transferred to silicon substrates for SEM imaging and AFM indentation purposes. More details about this technique can be found in the following Chapter 5.

4.3 Conclusion

In this work I demonstrated that self-assembled freestanding membranes could be bent controllably towards the water-facing side under electron-beam exposure. They can also spontaneously roll up due to water-induced swelling of the ligands at one side. Both processes produce rolled-up, hollow tube-like structures (nanoparticle scrolls). Indentation measurements on these nanoparticle scrolls are described in the next chapter where we use the results to study the bending stiffness of nanoparticle membranes.

4.4 References

1. Jiang, Z.; He, J.; Deshmukh, S. A.; Kanjanaboos, P.; Kammath, G.; Wang, Y.; Sankaranarayanan, S. R. S.; Wang, J.; Jaeger, H. M. & Lin, X. M. Subnanometre ligand-shell asymmetry leads to Janus-like nanoparticle membranes. *Nat. Mater.*, **14**, 912-917 (2015).

2. Zharnikov, M. & Grunze, M. Modification of thiol-derived self-assembling monolayers by electron and x-ray irradiation: Scientific and lithographic aspects. *J. Vac. Sci. Technol., B: Microelectron. Nanometer Struct. –Process., Meas., Phenom.*, **20**, 1793-1807 (2002).

3. Zhou, C.; Trionfi, A.; Hsu, J. W. P. & Walker, A. V. Electron-beam-induced damage of alkanethiolate self-assembled monolayers (SAMS): dependence on monolayer structure and substrate conductivity. J. Phys. Chem. C, **114**, 9362-9369 (2010).

4. Kanjanaboos, P.; Joshi-Imre, A.; Lin, X. M. & Jaeger, H. M. Strain patterning and direct measurement of Poisson's ratio in nanoparticle monolayer sheets. *Nano Lett.,* **11**, 2567-2571 (2011).

CHAPTER 5

BENDING RESISTANCE MEASUREMENTS IN NANOPARTICLE MEMBRANES[‡]

5.1 Introduction

Ultrathin sheets comprised of a few layers of atoms, such as graphene,[1-3] or a few layers of close-packed, ligated nanoparticles[4-12] have attracted much interest because of their unique properties. In terms of mechanical properties, most attention has focused on nominally flat sheets. These thin sheets have been found to be mechanically robust and remarkably stiff under extension, capable of forming large freestanding membranes.[5-7,10,13-15] However, out-of-plane bending, while playing a key role in emerging fields such as the manipulation of thin films into three-dimensional structures,[9,16-19] is just starting to be explored[3] in systematic experiments for ultrathin sheets. With thicknesses on the order of or below 10nm, such sheets are expected to be highly flexible and responsive to out-of-plane bending. The questions we are addressing here are to what extent the resistance to bending can be derived from knowledge of the physical thickness of the sheet and its tensile strength, and how can one extract the bending modulus.

In general, the resistance of a thin sheet to elastic deformation via stretching and bending is characterized by the in-plane, two-dimensional (2D) Young's modulus E_{2D} and by the out-of-plane bending modulus κ, respectively. These two parameters define an effective bending

[‡] This Chapter is largely based on Wang, Y.; Liao, J.; McBride, S. P.; Efrati, E. Lin, X. M. & Jaeger, H. M. Strong resistance to bending observed for nanoparticle membranes. *Nano Lett.*, **15**, 6732-6737 (2015).

thickness t_{eff} through the relationship $\kappa = \frac{E_{2D} t_{\text{eff}}^2}{12(1-\nu^2)}$, where ν is Poisson's ratio. E_{2D} is related to the bulk Young's modulus E via $E_{2D} = Et$, where t is the physical thickness of the sheet.

For homogeneous planar materials t_{eff} corresponds to the physical thickness t, but going beyond standard continuum elasticity t_{eff} can encapsulate effects due to deviations from planarity or from the continuum limit. The former occurs, for example, when thermal or quenched height fluctuations increase resistance to bending and thus the effective thickness,[3,20] similar to what happens in a crumpled sheet of paper, while the latter can occur when the physical thickness becomes close to the size of the constituent particles so that particle-scale features and any resulting (non-local) structural constraints need to be accounted for.[21-25] In either case, the experimental problem is that E_{2D} (or E) and κ are not simply related by the physical thickness t and thus need to be measured independently. This typically requires two distinct types of measurements probing separately the different modes of deformation in isolation.

Here we introduce an approach that circumvents this difficulty. As is the case for a thin, floppy sheet of paper, rolling up a monolayer into a hollow tube turns it into a stiffer and thus more easily probed structure. Importantly, the tube's response to small local indentations is a signature of contributions from both bending and stretching. As a result, a single set of measurements of the resistance to indentation along the length of a tube provides direct access to E_{2D} as well as κ.

5.2 Experiment Setup

As described in Chapter 4, there are several ways to bend freestanding nanoparticle sheets into tube-like structures. One is via exposure to an electron beam. Our previous work used electron-beam exposure to roll up freestanding monolayers into scrolls.[26,27] However, the e-beam also crosslinks the ligands and changes the mechanical properties.[14] In the experiments discussed here, an alternative, non-invasive method is used, whereby nanoparticle monolayers curl up spontaneously (Figure 5.1).

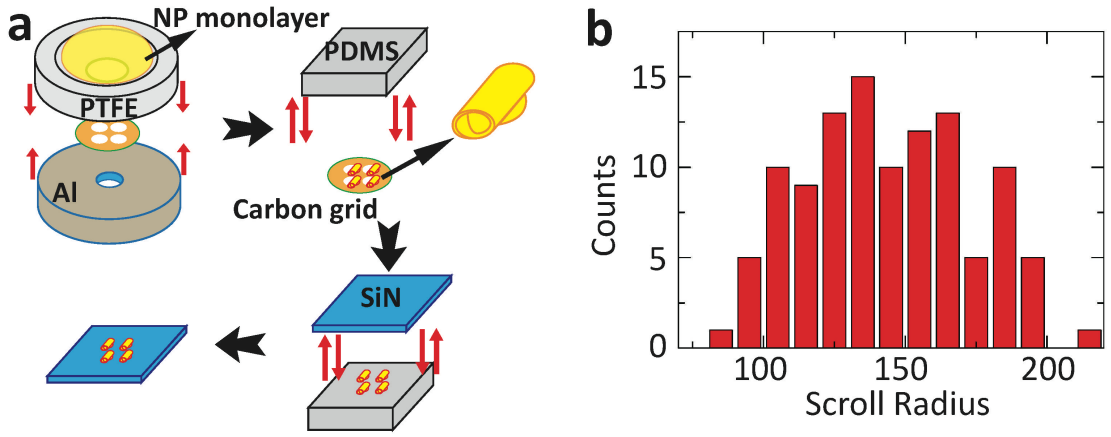

Figure 5.1 Self-assembly and transfer of nanoparticle scrolls. **a**, Schematic of fabrication steps. Nanoparticle monolayers are assembled at the air-water interface in a PTFE holder and dried onto a carbon TEM grid containing 2μm diameter holes placed at the bottom of the holder. Right after the water dewets the carbon grid, weak nanoparticle membranes partially detach from the holes' rims and spontaneously roll up. By gently contacting the scrolls with a PDMS stamp, they can be pulled off the carbon grids and transferred to Si/SiN wafers that have been coated with dodecyltrichlorosilane. Due to stronger adhesion to the silane than to the PDMS, the scrolls stick to the wafer. **b**, Histogram of the scroll radius distribution. The radius R is determined by the strain gradient across the monolayer prior to curling up. From the average $R \approx 150$nm we estimate an initial strain difference $\Delta\varepsilon = \frac{t_0}{R} \approx 5\%$ between the two sides of a monolayer. This is based on an average monolayer thickness $t_0 = 7$nm, as obtained from AFM measurements on multilayers of the same particles but deposited on flat surfaces.

Dodecanethiol ligand-capped gold nanoparticles with diameters of (5.2 ± 0.3)nm, suspended in toluene, were synthesized using a digestive ripening method.[28] Monolayers were assembled by adding 8μL of nanoparticle solution onto a 100μL distilled water droplet deposited in a cone-shaped PTFE holder (Figure 5.1a, alternative droplet drying methods[13] can also be used create scrolls under appropriate thiol conditions). A carbon grid (Quantifoil 657-200-CU from Ted Pella) with 2μm diameter circular holes was clamped between the PTFE holder and an aluminum disk, and the nanoparticle monolayer eventually deposit onto the carbon grid after the water droplet evaporated. The mechanical strength of the resulting freestanding sheets inside the holes was adjusted by carefully tuning the ligand concentration in the solvent such that they tended to detach along one side of a hole as the last remaining water evaporated underneath. Partially detached monolayers spontaneously rolled up toward the air-facing side (the opposite direction of previously observed electron beam induced folding[26,27]), resulting in multi-layered nanoparticle scrolls, as imaged by a Joel 2100F transmission electron microscope (Figures 5.2a,b) and a FEI Nova NanoLab SEM (Figures 5.2c,d). We believe this curling is driven by residual water trapped preferentially in the ligands of the originally water-facing side of the monolayers: water has a larger modulus than the alkanethiol ligands and thus the bottom side of a monolayer in contact with water relaxes less when the membrane detaches and its draping-induced prestrain is released. This is supported by the fact that spontaneous curling did not occur when monolayers detached (or were strain relieved by ion beam cutting[27]) *after* having fully dried.

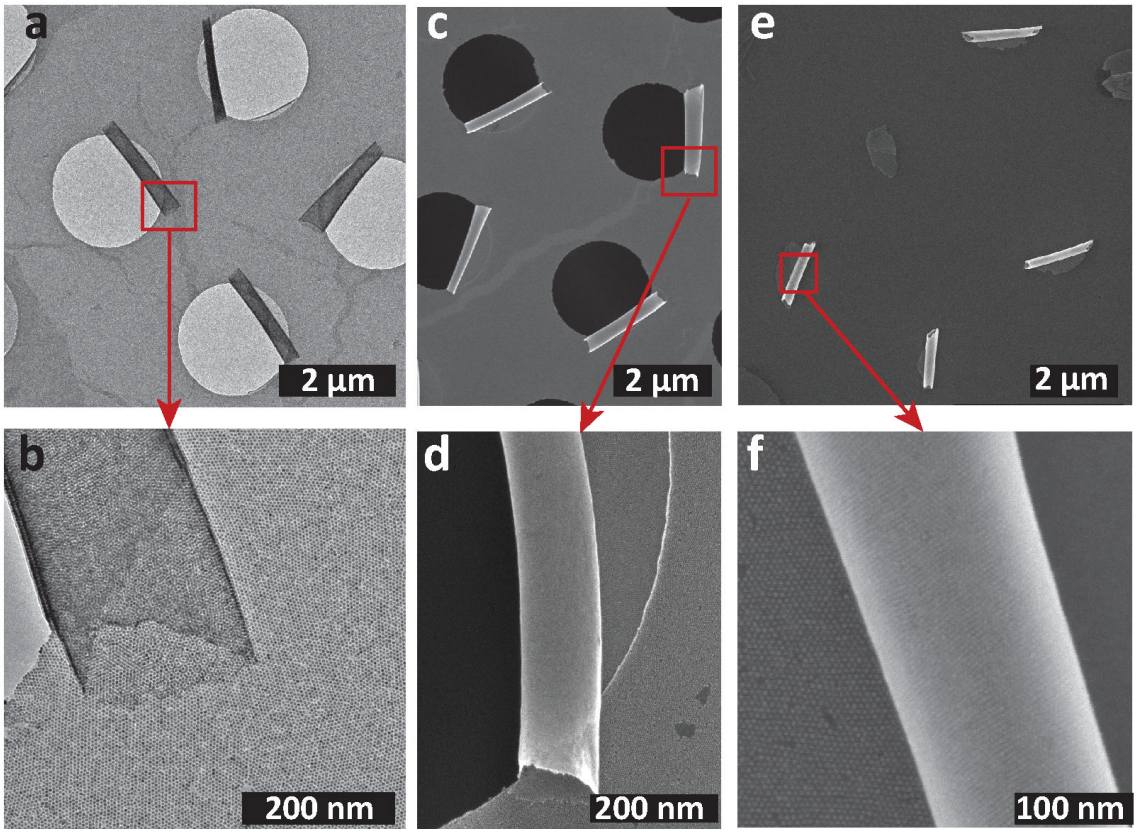

Figure 5.2: **(a, b)** TEM images of free-standing nanoparticle scrolls on a holey carbon grid. Individual nanoparticles with ≈5.2nm diameter can be resolved. Due to the circular shape of the original monolayer piece that curled up, the wall thickness increases toward the scroll center, but the portions extending beyond the hole remain the thinnest. **(c, d)** SEM images of nanoparticle scrolls on a holey carbon grid. **(e, f)** SEM image of nanoparticle scrolls after transfer.

Polydimethylsiloxane (PDMS) stamps were used to transfer the scrolls from the carbon grids to SiN/Si substrates (Si coated with 50-100nm of SiN). The substrate surfaces were modified by coating them with dodecyltrichlorosilane (Sigma-Aldrich) to enhance sticking of the scrolls after transfer. The PDMS stamps were made by mixing the base and curing agent (SYLGARD 184 Silicone Elastomer Kit, Fisher Scientific) with a ratio of 7:1, followed by degassing and curing at 70 °C for one hour. Since the elastic modulus of the nanoparticle scrolls exceeds that of PDMS by more than a factor of a thousand,[5,13,15] most of the deformation during stamping took place inside the PDMS, and the scrolls showed no evidence of crumpling, collapse, or other

irreversible plastic deformation. However, we found that the pressure from the PDMS stamp shears off the single-layered sections that extend over the hole at both ends of a scroll (the ends are necessarily single-layered because the scrolls form by rolling up circular sheets; Figures 5.2a-d). Therefore, only the central, multi-layered part of the scrolls was transferred onto the wafer (see Figures 5.3&5.4). The radii *R* of over 100 measured scrolls ranged from 50nm to 250nm, with mean ~150nm, as determined by SEM (Figures 5.2e,f). Given 2μm diameter circular sheets as starting material, this implies a final scroll wall thickness of 2-3 monolayers (Figure 5.3&5.4).

In order to understand the formation process of the nanoparticle scrolls and their internal geometries, I made paper scrolls that resemble the scroll geometry obtained from nanoparticle membrane experiments that will be studied in the following. These paper scrolls are shown in Figure 5.3&5.4 below.

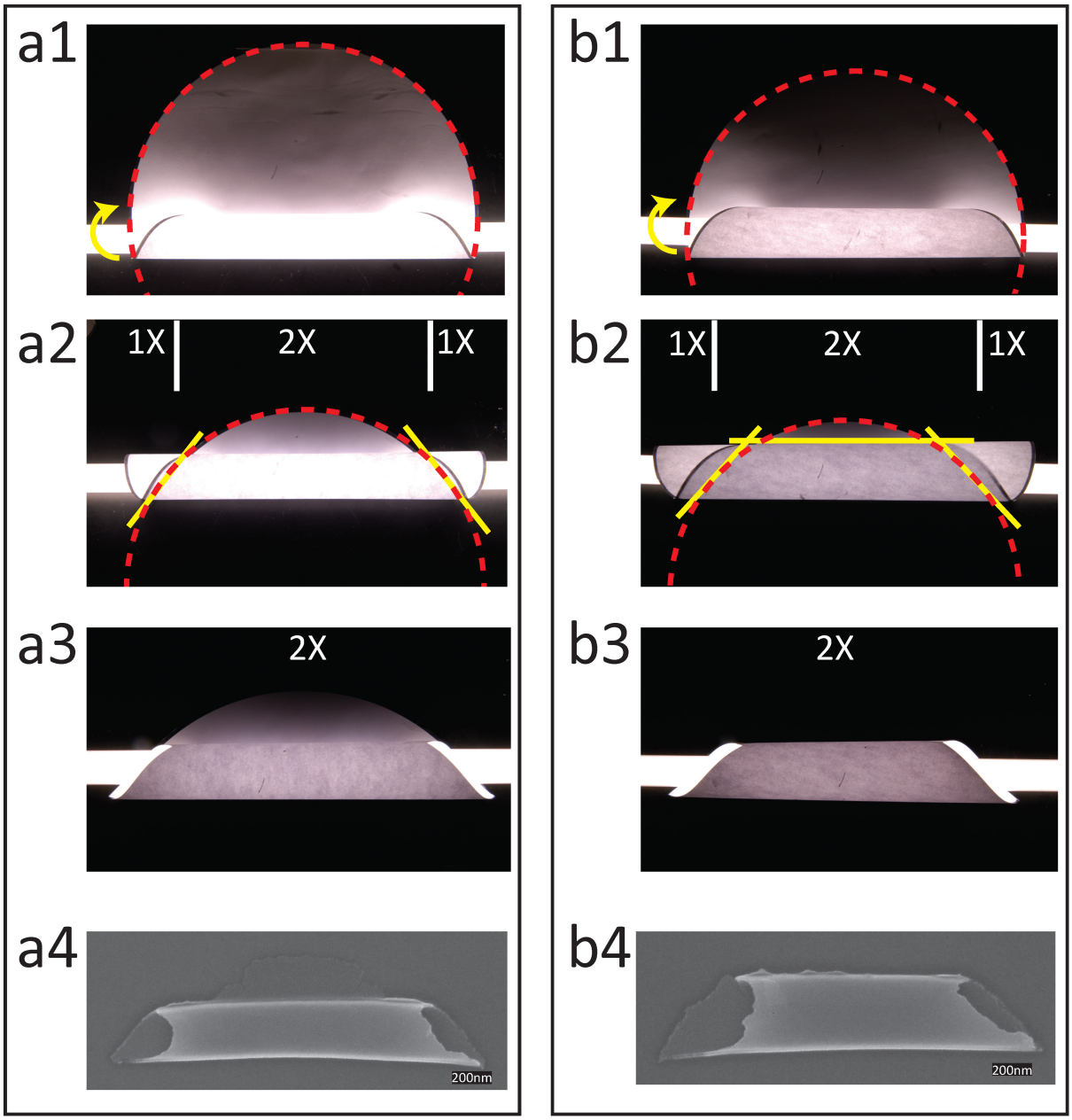

Figure 5.3 Paper models corresponding to the nanoparticle scrolls in the Figure 5.7a&b, demonstrating how their internal structure arises.

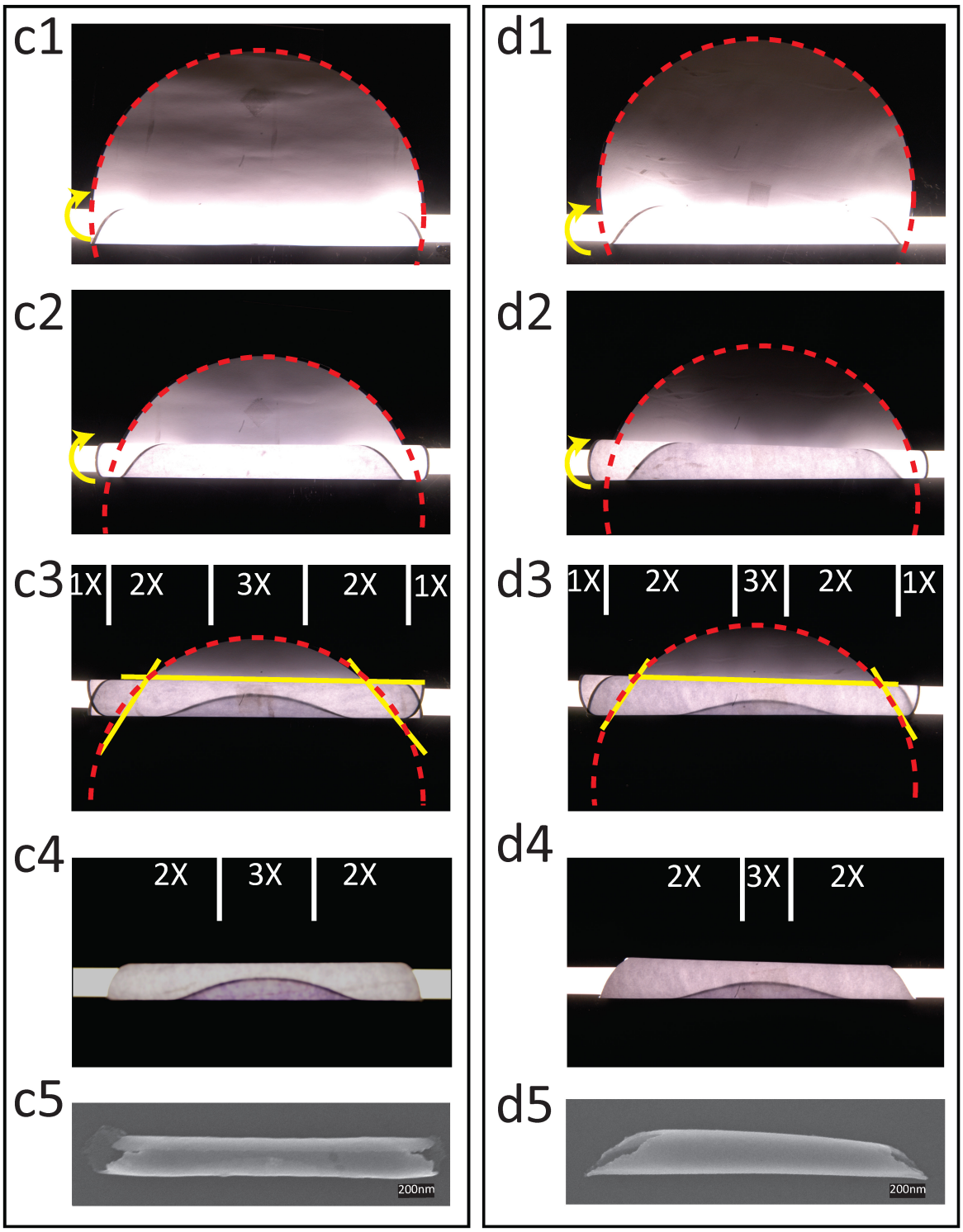

Figure 5.4 Paper models corresponding to the scrolls in Figure 5.7c&d, demonstrating how their internal structure arises.

All images in Figure 5.3 are top views. The sequence of images in each column reads from top to bottom; the last image in each column is an SEM image of the actual scroll. The paper scrolls were made by rolling up a circular piece of paper of diameter 200mm, corresponding to the 2μm diameter circular nanoparticle sheet. The images are taken with the rolled up paper on a black table to enhance contrast, the bright horizontal bars are fluorescent tubes placed inside the paper scrolls to reveal the scroll wall structure. The red dashed line indicates the perimeter before the paper was rolled up. The white numbers at the top of the images indicate the number of resulting layers along the top ridge of the scroll. The yellow lines show where the paper scroll was cut, mimicking the shearing-off process during the nanoparticle scroll stamping, when the PDMS stamp pushes the rolled up scroll against the substrate and the hole perimeter acts as a knife edge. This demonstrates why the single-layer sections at both scroll ends are missing after the transfer to the Si substrate. As the paper models verify, the final rolled-up geometry of both scrolls is such that the wall thickness at the top is 2 layers along the full length.

The same comments as for Figure 5.3 apply to Figure 5.4, except that for these two scrolls there is a middle section comprised of a partial third layer in the interior of the scrolls. The geometry of this partial layer is seen in panels c4 and d4. The 'lip' shape of this extra layer indicates that it is the very first part of the sheet that spontaneously rolled up, and its exact position depends on how far the sheet rolled (which we can determine by the scroll position with respect to the edge of the hole, as in panels c3 and d3, or indirectly by the length of the scroll. The partial third layer is taken into account in the simulations shown in later figures and discussions shown in this Chapter.

Figure 5.5 shows examples of nanoparticle scrolls imaged and indented by an Asylum MFP3D atomic force microscope (AFM) equipped with AppNano ACTA cantilevers. In all cases, the maximum indentation applied was less than 10nm, which is below the wall thickness of the scroll, to avoid buckling.[29,30] Using AFM, we found that height variations along the longitudinal direction of scroll surface stayed within 1-2 particle diameters, indicating that thermal shape fluctuations or quenched crinkles[3] are most likely not relevant. The indentation curves were essentially linear, with little hysteresis between indentation and retraction, implying the deformation was small enough to stay in the linear elastic regime. The local stiffness k, i.e., the local effective spring constant, was calculated from the slope of force curves as in Figure 5.3b, and a stiffness map was obtained.

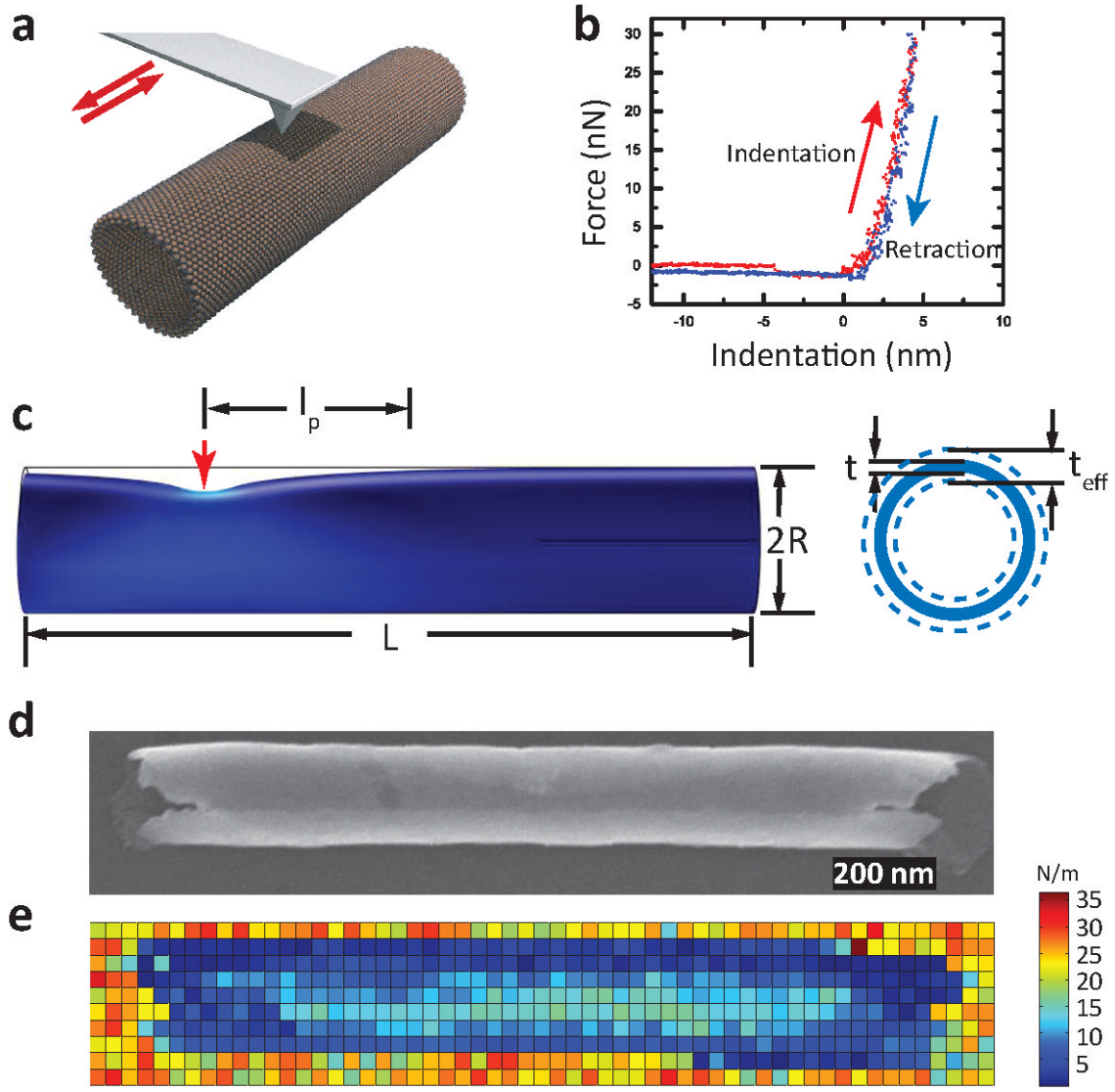

Figure 5.5 Indentation stiffness maps. **a**, Illustration of an AFM cantilever tip scanning and indenting a nanoparticle scroll. **b**, Typical force-indentation curve taken at the center of a scroll. **c**, Sketch of a tube deformed after indentation (left) and its cross section. The side view on the left is obtained from a COMSOL simulation of a thick tube indented at the red arrow. The parameters l_p, R and L are identified. The cross section on the right shows the physical thickness t and effective thickness t_{eff} for bending. **d**, SEM image of a nanoparticle scroll (radius R=90nm, length L=1.7 μm). **e**, Stiffness map of the scroll in **d**. To obtain the stiffness map, the MFP3D AFM was programmed to indent at a grid of points within a selected rectangular area above a scroll's central axis. The indentation targets were spaced ≈37nm both in the axial, x-direction and the transverse, y-direction, resulting in a force-indentation map of 57×10 pixels over a 2.1μm x 0.37μm area. The stiffness values at each point were calculated from a linear fit to the indentation approach data, using a Matlab script. Note that along the direction transverse to the central x-axis, the decrease of stiffness to either side of the scroll apex is caused by some slip of the AFM tip when the tip trajectory is not perpendicular to the scroll surface. Therefore, only values within close proximity of the x-axis were used for analysis. Note also the larger stiffness

along the top ridge of the scroll and the drop-off near the open ends. The AppNano ACTA cantilevers used here have a measured resonance frequency of ~300 kHz and a spring constant of 14 N/m to 20 N/m, which matches the stiffness of the scrolls. The orange/red colors reflect the larger stiffness of the substrate (given our particular AFM cantilever, with its stiffness appropriately matched to that of the scroll, those values are beyond the range of reliable measurement).

5.3 Results and Discussion

The resulting map (Figure 5.5e) exhibits several important features. First, the stiffness values, ranging from 10 - 30N/m, are relatively large, comparable to the resistance to in-plane stretching.[5,13] Second, along the central axis, where the tip is indenting perpendicular to the scroll surface, the stiffness profile *k(x)* reflects details of the tubular geometry that resulted from the roll-up process.

In order to understand the stiffness variation along the central axis, the concept of the indentation persistence length needs to be introduced. This persistence length characterizes the spatial extent of a small local deformation (see Figure 5.5c), and its value[31] $l_p \approx 4.4R^{3/2}/t_{\text{eff}}^{1/2}$ is the result of balancing out-of-plane bending and in-plane stretching energies inside the rolled-up sheet. In the thin-wall limit $t_{eff} \ll R$, l_p can become larger than the scroll length L, in which case the deformation is global and mostly due to bending. As a result, the stiffness profile *k(x)* shows a single peak at the center, and a slow monotonic drop-off to either side that arises from non-affine deformation involving the whole tube length.

As the walls become thicker, stretching starts to contribute significantly and the deformation becomes localized to a finite zone of extent $l_p < L$. Integrating both contributions across the deformation zone and minimizing the total energy results in an *x*-independent stiffness given by[29]

$$k = 1.18E_{2D}\left(\frac{t_{eff}}{R}\right)^{3/2} \tag{5.1}$$

In this limit the stiffness depends on the local radius *R* and the local effective thickness t_{eff}, rather than on the global structure of the scroll. Only once the indenter gets to within l_p from a change in R or t_{eff}, for example near either end of the tube, does the deformation energy, and thus the stiffness, change.

Based on these considerations, the ratio l_p/L determines the stiffness profile *k(x)* along the central axis of a tube, while E_{2D} only sets the overall scale. By analyzing experimental stiffness profiles as in Figure 5.5, and comparing them to finite element simulations of the experimental tube geometries (Figure 5.6), we can extract information about the persistence length l_p and calculate the effective wall thickness t_{eff}. Given t_{eff}, we then obtain E_{2D} and from it the bending modulus κ.

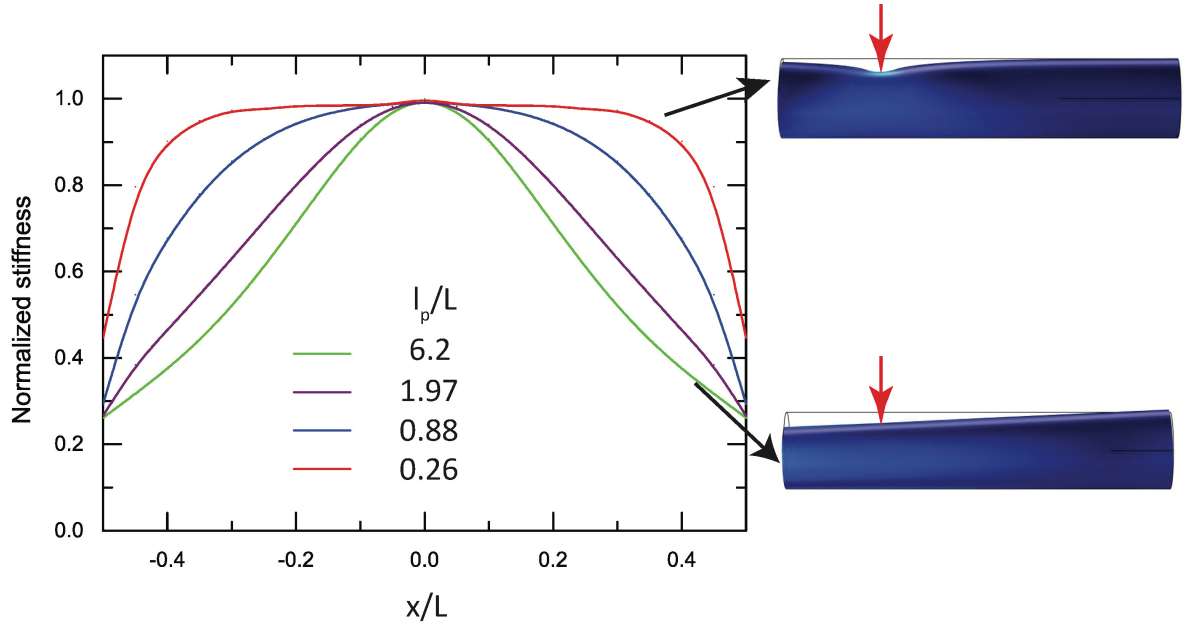

Figure 5.6 Finite element simulation results for different l_p/L parameters. Normalized stiffness $k(x)/k(0)$ versus normalized axial indentation position x/L are plotted for tubes with a range of l_p/L ratios. As discussed in the text, l_p/L fully determines the shape of the stiffness profile $k(x)$ of a tube along its length. The two insets are simulation figures of tubes with small l_p/L ratio (0.26, bottom) and large l_p/L ratio (6.2, top). As demonstrated by this figure we can extract the l_p/L value from matching the measured and simulated stiffness profiles, and use that to calculate the effective thickness t_{eff}.

Finite element simulations of the stiffness profiles were conducted with COMSOL Multiphysics 5.1, using the structural mechanics module. For these simulations, the overall scroll geometry was obtained from SEM or AFM images; the internal scroll geometry, and in particular the local (physical) wall thickness, was reconstructed from models as shown in Figures 5.3&5.4. A scroll was then modeled as an axial stack of bonded tube sections of appropriate wall thickness, accounting in cases such as Figure 5.4 for the fact that an extra (here: third) layer might be present only across a portion of a tube section.

From images of individual scrolls together with the associated portions of monolayer that have not curled up, we can find the internal scroll geometry and reconstruct the local wall thickness as

a function of axial coordinate x (Figures 5.3&5.4). If we use the physical thickness, which is a multiple of the nanoparticle monolayer thickness t_0 = 7nm, to calculate the persistence length, we find that all nanoscrolls should be within the thin-wall limit and we would therefore expect that local indentation should lead to global deformation. For example, the scroll shown in Figure 5.7a has radius R =150nm and wall thickness $t = 2t_0$, which gives $l_p \approx 2.1\mu m$, larger than the scroll length L = 1.4μm. The blue trace in that figure shows the corresponding, predicted axial stiffness profile $k(x)$, obtained from the finite element calculation.

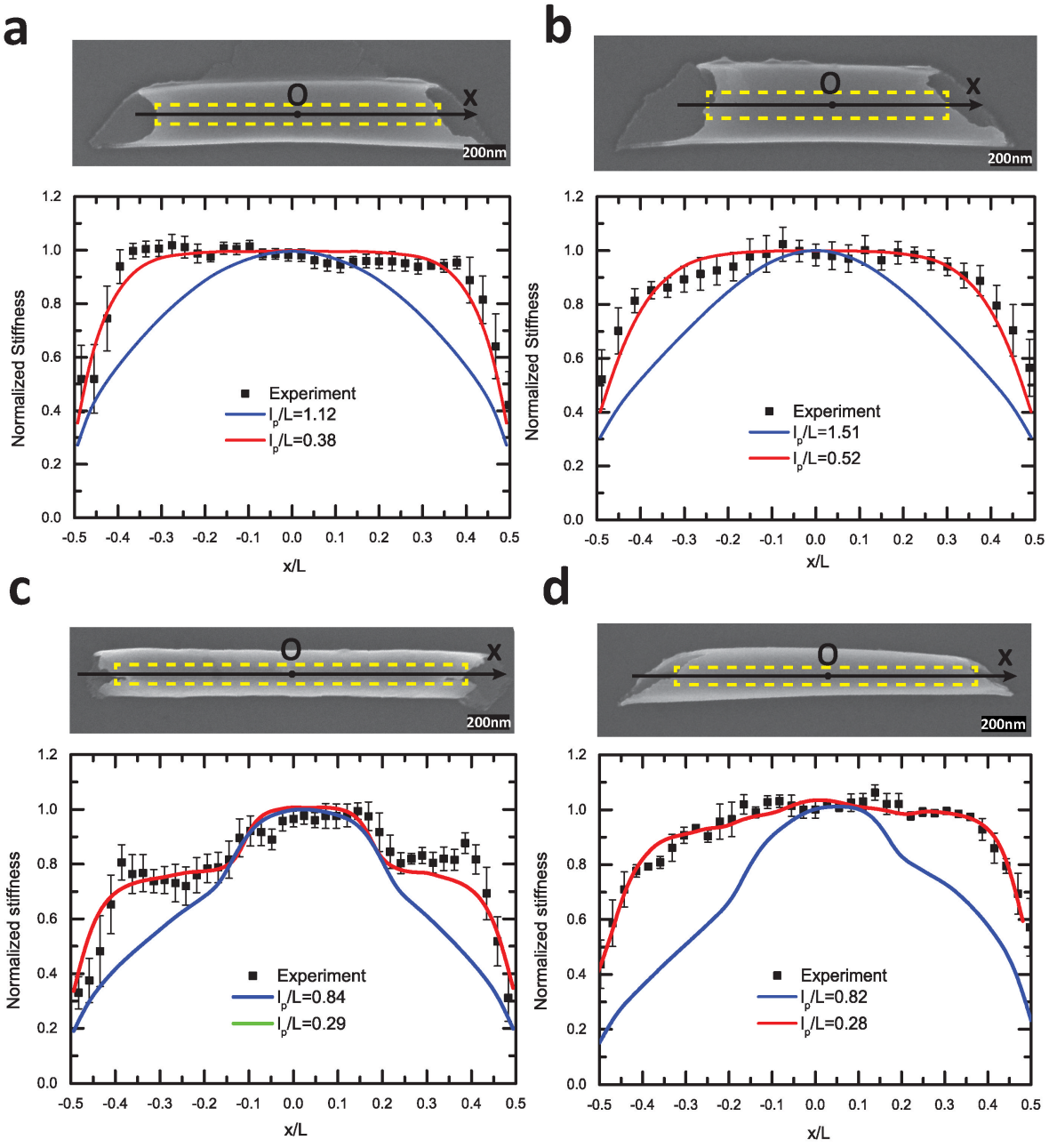

Figure 5.7 Axial stiffness profiles of scrolls with various geometries. Experimental data are represented by black square points, with error bar coming from the standard deviation of neighboring pixel values from the stiffness map. These profiles contain signatures both of the scroll geometry and of the interplay between resistance to stretching and to bending. The local stiffness of a scroll of length L is normalized by its average value at the center (x = 0). The persistence length l_p characterizes the size of the deformation zone due a local indentation. Four examples are shown of scrolls that differ in l_p/L ratio, shape (cylindrical, conical), and wall thickness. **(a)**, Cylindrical scroll (R = 150nm, L = 1.39μm) with uniform wall thickness of 2 monolayers along the top. **(b)**, Cylindrical scroll (R = 180nm, L = 1.22μm) with uniform wall thickness of 2 monolayers along the top. **(c)**, Cylindrical scroll (R = 105nm, L = 1.7μm) with

Figure 5.7, continued. wall thickness of 2 monolayers at the ends and 3 layers at the center. **(d)**, Cone-shaped scroll (135nm > R > 80nm, L = 1.5μm) with uniform wall thickness of 2 monolayers at the ends and 3 layers at the center. The shaded rectangular region in the SEM images of the scrolls indicates the area over which the stiffness data was taken and locally averaged. Each data point was averaged among a neighboring 110nm x 74nm area from the stiffness map (see Figure 2e), the size of the error bars on the plotted experimental data (black squares) corresponds to one standard deviation around the mean. Solid curves are finite element simulations for different values of l_p/L, which depends on wall thickness. Using the physical thickness t predicts spatially extended deformation zones and significant end effects (blue) incompatible with the experimental data, which, however, can be reproduced well by assuming a large effective thickness t_{eff} (red). The best-fit ratio $t_{\text{eff}}/t \approx 9$ indicates an enhancement of the bending modulus by almost two orders of magnitude over predictions from standard continuum elasticity.

The striking discrepancy with the experimental data in Figure 5.7a demonstrates that nanoparticle scrolls resist indentation as if they had a wall thickness $t_{\text{eff}} >> t$. Best fits of the data to finite element simulations give $l_p/L \approx 0.4$, which implies $t_{\text{eff}} \approx 120$nm or almost 9 times the physical thickness. This large t_{eff} should be viewed as proxy for an unusually large ratio of bending to stretching moduli, *i.e.*, of resistance to bending which far exceeds that expected from a description of the monolayer as homogeneous continuum material.

We find the same qualitative behavior in all nanoparticle scrolls measured. This includes scrolls with larger aspect ratio of R/L (Figure 5.7b) as well as scrolls with non-uniform wall thickness along their apex (Figure 5.7c), where the larger stiffness in the center portion arises from the presence of a third layer in the hollow interior underneath the apex (the 'lip' portion of the circular sheet at the beginning of the scroll formation). In Figure 5.7d we show the stiffness profile for a cone-shaped scroll with non-uniform radius along the axis, with higher stiffness towards the smaller radius, in accordance with Eq. 1. For scrolls in Figures 5.7a&b, using t_{eff} = 120nm in the bilayer provides consistently good fits (red traces in Figure 5.7), while using the physical thickness of 14nm clearly does not (blue traces).

Note that t_{eff} in this way is extracted from the *shape* of *k(x)* alone, independent of the value of E_{2D} (see Figure 5.6). The 2D modulus E_{2D} is then found from matching the experimentally measured stiffness in the center of the scroll, *k(0)*, to finite element simulations or, for $l_p \ll L$, directly using Equation 5.1. For scrolls with varying local wall thickness this holds as long as we can assume that the Young's modulus E is independent of wall thickness, so that $E_{2D} = Et$ applies. For our scrolls, t_{eff} and R are of similar magnitude and thus, via Eq. 1, the same is true for k and E_{2D}. Indeed, the experimental *k(0)* values of 10-30N/m in the central, 2-layered scroll sections are reproduced by the simulations with E_{2D} ranging from 34-65 N/m. Using $t = 14\mathrm{nm}$ this implies Young's moduli E around 2-4 GPa, fully consistent with prior measurements using stretching.[5,11]

With $t_{\mathrm{eff}} = 120\mathrm{nm}$ the bending modulus of a bilayer wall is $\kappa = \frac{E_{2D}t_{eff}^2}{12(1-\nu^2)} \approx 4\times10^5\mathrm{eV}$, where we used $\nu = 0.3$ from earlier measurements.[14] This value for κ is about two orders of magnitude larger than had we used the physical thickness t, which would give $\kappa_0 \approx 6\times10^3\mathrm{eV}$. This breakdown of classical continuum elasticity signals the importance of taking into account the discrete, finite size nature of the constituent units as well as any structural heterogeneity in ultrathin nanoscale systems. Both can result in non-local coupling of rotational degrees of freedom.[21-25] We note that the in-plane behavior, and thus E_{2D}, is not affected since no particle rotation is involved during planar stretching. The general result is a correction to the bending modulus given by[21,23]

$$\kappa = \kappa_0 \left[1 + 6(1-\nu)\left(\frac{l}{t}\right)^2\right], \tag{5.2}$$

which can become dominant when t falls below a material-specific length l. For our experiments with bilayer walls, $\kappa/\kappa_0 = (t_{\text{eff}}/t)^2 \approx 9^2$ implies $l \approx 60\text{nm}$, a distance of roughly 8-9 particle diameters. l is the length scale at which classical elasticity breaks down for the specific material[24]. In our nanoparticle membranes, we expect l to change with nanoparticle sizes, the type of ligands between particles, and the crystalline grain sizes in the membranes.

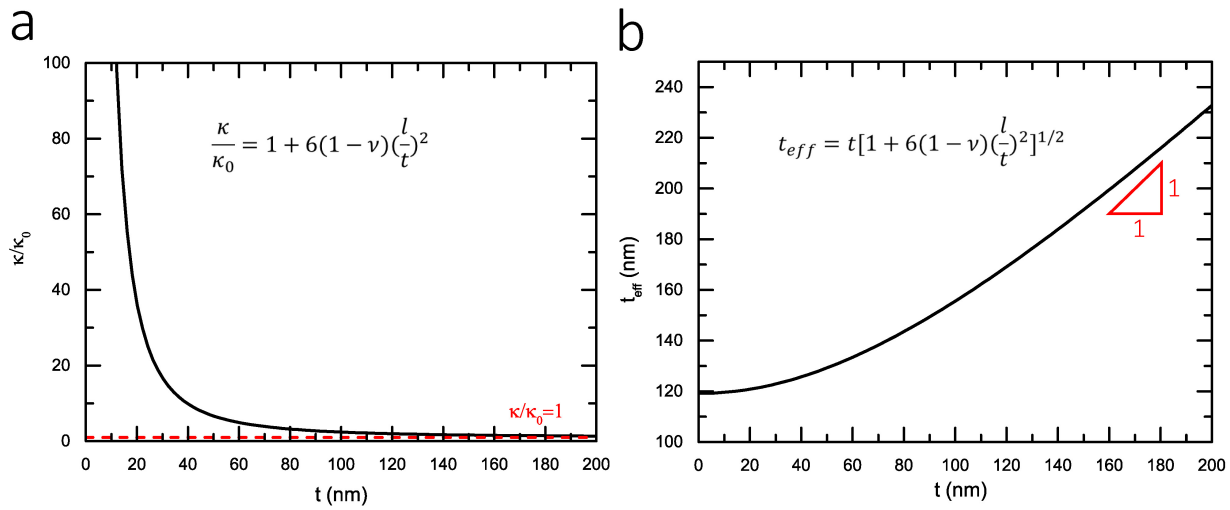

Figure 5.8 κ/κ_0 and t_{eff} as function of the physical thickness t. The plots show the predictions of Eq. 5.2, using numerical values (l = 60nm and ν = 0.3**)** appropriate for our experiments**. a,** The ratio between modified and classical bending stiffness. At small t, the mismatch between κ and κ_0 is large, while these two eventually converge for very large t. **b**, Effective thickness t_{eff}. At small t, t_{eff} levels off at $2l$, while the two thickness become equal at large t.

κ/κ_0 and t_{eff} as function of the physical thickness t predicted by this equation is shown in Figure 5.8. An easily testable prediction of Equation 5.2 is that, once $t \ll l$, the effective thickness t_{eff} should stop changing with physical thickness and level off at $t_{\text{eff}} \approx 2l$. Specifically, Equation 5.2 predicts that going from 2-layer (14nm) to 3-layer (21nm) sections of scrolls as in Figures 5.7c&d changes t_{eff} by less than 1%. Simulations based only on the scroll geometry and using the same $E = E_{2D}/t$ and same $t_{eff} = 120\text{nm}$ for both the 2- and 3-layer sections, with no

further adjustable parameters, indeed reproduce the experimental data extremely well (red traces in Figures 5.7c&d).

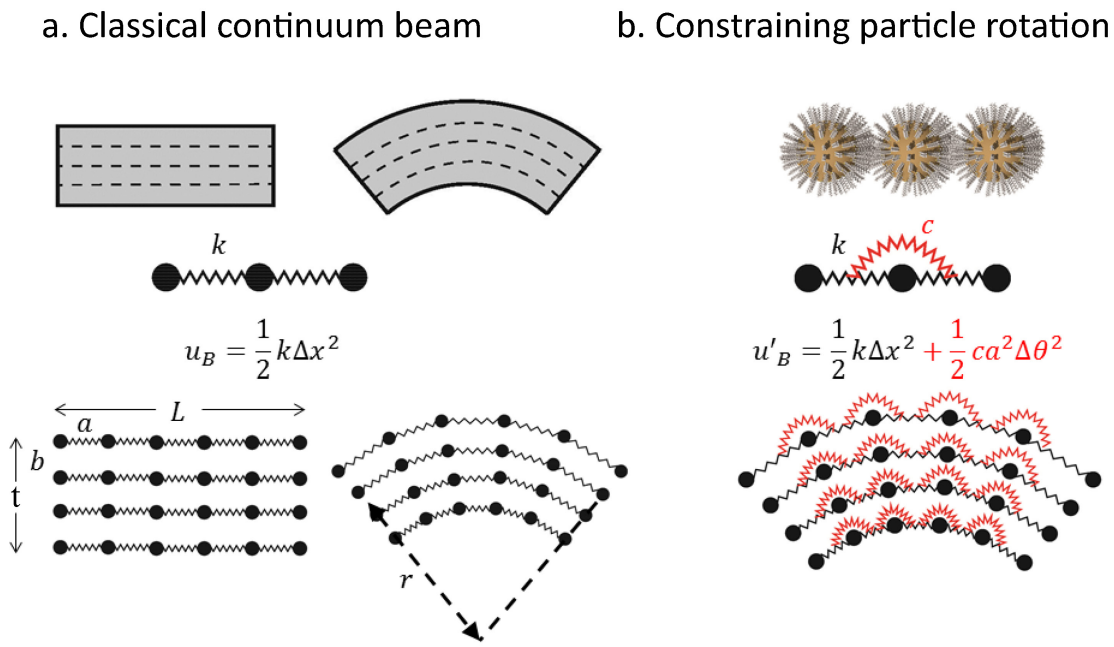

Figure 5.9 Ball and spring models for the bending of classical continuum beams (**a**) and for membranes with microstructure (**b**).

In order to explain these deviations of experimental results from classical continuum elasticity, we introduce a simple (toy) model by introducing nonlocal interactions. For the classical continuum beam with dimensions shown in Figure 5.9, the elastic energy for pure bending can be calculated by integrating the elastic energy for all springs:

$$U_B = \frac{kaL}{24b} \cdot \frac{t^3}{r^2} \tag{5.3}$$

where t is the physical thickness. Here all springs are assumed to be able to pivot freely around their endpoints.

If particles are constrained in their ability to rotate out of the plane of their neighbors, we can mimic this by adding a torsional spring (with spring constant *c*), as shown in Figure 5.9**.** We assume that this spring does not resist changes in particle separation, but is directly affected by curvature. In the experimental system this behavior would arise from the specifics of the particle shape and its ligand covering, and it would be one possible type of ligand-mediated coupling beyond nearest neighbor particles. The energy for bending can then be calculated as**:**

$$U_B' = \frac{kaL}{24b} \cdot \frac{t^3}{r^2} + \frac{ca^3L}{2b} \cdot \frac{t}{r^2} = U_B \cdot (1 + \frac{12c}{k} \cdot \frac{a^2}{t^2}) \tag{5.4}$$

In thick films, *t* is much larger than the inter-particle spacing *a*, and the second term becomes small. As a result, the bending energy approaches the classical limit. However, in films where t is comparable to *a*, the second term can be large and even dominate, making the bending energy larger than predicted by classical theory. Since the bending energy scales with the bending stiffness, we obtain for the stiffness

$$\kappa = \kappa_0(1 + \frac{12c}{k} \cdot \frac{a^2}{t^2}) \tag{5.5}$$

Comparing this to equation (2) in the main text we can express the length *l* as

$$l = [\frac{2c}{(1-\nu)k}]^{1/2} a \tag{5.6}$$

Within this simple model, the non-local length scale is related to both out-of-plane bending and in-plane stretching constraints on particles via the spring constants c and k. Using the experimental values $l \approx 60nm$ and $a \approx 7nm$, we obtain $c/k \approx 25$ for the relative strength of out-of-plane to in-plane constraints.

5.4 Conclusion

These results constitute the first direct measurements of the bending modulus for nanoparticle membranes. While the membranes are obviously quite flexible because they are so thin, their resistance to bending is nevertheless much larger than standard elasticity would predict based on the in-plane stretching behavior. Such remarkably strong enhancement of κ indicates that understanding out-of-plane bending in these systems necessitates new considerations. At this stage, it remains an open question how the large κ/κ_0 ratio arises from non-local, ligand-mediated interactions between nanoparticles. In Figure 5.9 we show that some aspects related to increasing t_{eff} can be captured by a simplified model. More detailed insights are likely to require extensive molecular dynamics simulations, such as those recently employed to investigate stretching of planar layers.[11] By varying ligand length and nanoparticle shape it should be possible control t_{eff} and thus tailor κ and $E_{2\mathrm{D}}$ independently, an intriguing option for nanomechanical systems. The new method introduced here for obtaining both stretching and bending moduli from a single set of indentation measurements coupled with finite element simulations circumvents the traditional requirement of separate experiments. Since the method is only based on the tube geometry and elastic theory, it should have general applicability across a wide range of materials and size scales.

5.5 References

1. Bunch, J. S.; Zande, A. M.; Verbridge, S. S.; Frank, I. W.; Tanenbaum, D. M.; Parpia, J. M.; Craighead, H. G. & McEuen, P. L. Electromechanical resonators from graphene sheets. *Science*, **315**, 490 (2007).

2. Lee, C.; Wei, X.; Kysar, J. W. & Hone, J. Measurement of the elastic properties and intrinsic strength of monolayer graphene. *Science*, **321**, 385 (2008).

3. Blees, M. K.; Barnard, A. W.; Rose, P. A.; Roberts, S. P.; McGill, K. L.; Huang, P. Y.; Ruyack, A. R.; Kevek, J. W.; Kobrin, B.; Muller, D. A. & McEuen, P. L. Graphene Kirigami. *Nature*, **524**, 204-207 (2015).

4. Lin, Y.; Skaff, H.; Böker, A.; Dinsmore, A. D.; Emrick, T. & Russell, T. P. Ultrathin cross-linked nanoparticle membranes. *J. Am. Chem. Soc.*, **125**, 12690-12691 (2003).

5. Mueggenburg, K. E.; Lin, X. M.; Goldsmith, R. H. & Jaeger, H. M. Elastic membranes of close-packed nanoparticle arrays. *Nat. Mater*., **6**, 656-660 (2007).

6. Cheng, W.; Campolongo, M. J.; Cha, J. J.; Tan, S. J.; Umbach, C. C.; Muller, D. A. & Luo, D. Free-standing nanoparticle superlattice sheets controlled by DNA., *Nat. Mater*., **8**, 519-525 (2009).

7. Dong, A.; Chen, J.; Vora, P. M.; Kikkawa, J. M. & Murray, C. B. Binary nanocrystal superlattice membranes self-assembled at the liquid-air interface. *Nature*, **466**, 474-477 (2010).

8. Olichwer, N.; Leib, E. W.; Halfar, A. H.; Petrov, A. & Vossmeyer, T. Cross-linked gold nanoparticles on polyethylene: resistive responses to tensile strain and vapors. *ACS Appl. Mater. Interfaces*, **4**, 6151-6161 (2012).

9. Pham, J. T.; Lawrence, J.; Lee, D. Y.; Grason, G. M.; Emrick, T. & Crosby, A. Highly stretchable nanoparticle helices through geometric asymmetry and surface forces. *Adv. Mater.*, **25**, 6703-6708 (2013).

10. Rupich, S. M.; Castro, F. C.; Irvine, W. T. M. & Talapin, D. V. Soft epitaxy of nanocrystal superlattices. *Nat. Commun.*, **5**, 5045 (2014).

11. Salerno, K. M.; Bolintineanu, D. S.; Lane, J. M. D. & Grest, G. S. High strength, molecularly thin nanoparticle membranes. *Phys. Rev. Lett.*, **113**, 258301 (2014).

12. Liao, J.; Blok, S.; Molen, S. J.; Diefenbach, S.; Holleitner, A. W.; Schönenberger, C.; Vladyka, A.; Calame, M. Ordered nanoparticle arrays interconnected by molecular linkers: electronic and optoelectronic properties. *Chem. Soc. Rev*., **44**, 999 (2015).

13. He, J.; Kanjanaboos, P.; Frazer, N. L.; Weis, A.; Lin, X. M. & Jaeger, H. M. Fabrication and mechanical properties of large-scale freestanding nanoparticle membranes. *Small*, **6**, 1449-1456 (2010).

14. Kanjanaboos, P.; Joshi-Imre, A.; Lin, X. M. & Jaeger, H. M. Strain patterning and direct measurement of Poisson's ratio in nanoparticle monolayer sheets. *Nano Lett*., **11**, 2567-2571 (2011).

15. Wang, Y.; Kanjanaboos, P.; Barry, P.; Mcbride, S.; Lin, X. M. & Jaeger, H. M. Fracture and failure of nanoparticle monolayers and multilayers. *Nano Lett*., **14**, 826-830 (2014).

16. Guo, X.; Li, H.; Ahn, B. Y.; Duoss, E. B.; Hsla, K. J.; Lewis, J. A. & Nuzzo, R. G. Two- and three- dimensional folding of thin film single-crystalline silicon for photovoltaic power applications. *Proc. Natl. Acad. Sci. U. S. A*., **106**, 20149-20154 (2009).

17. Chun, I. S.; Challa, A.; Derickson, B.; Hsia, A. J. & Li, X. Geometry effect on the strain-induced self-rolling of semiconductor membranes. *Nano Lett.*, **10**, 3927-3932 (2010).

18. Ionov, L. Soft microorigami: self-folding polymer films. *Soft Matter*, **7**, 6786-6791 (2011).

19. Yao, K.; Manjare, M.; Barrett, C. A.; Yang, B.; Salguero, T. T. & Zhao, Y. Nanostructured scrolls from graphene oxide for microjet engines. *J. Phys. Chem. Lett*., **3**, 2204-2208 (2012).

20. Nelson, D. R. & Peliti, L. Fluctuations in membranes with crystalline and hexatic order. *J. Phys. (Paris)*, **48**, 1085-1092 (1987).

21. Yang, F.; Chong, A. C. M.; Lam, D. C. C.; Tong, P. Couple stress based strain gradient theory for elasticity. *Int. J. Solids Struct.,* **39**, 2731-2743 (2002).

22. McFarland, A. W. & Colton, J. S. Role of material microstructure in plate stiffness with relevance to microcantilever sensors. *J. Micromech. Microeng.*, **15**, 1060-1067 (2005).

23. Park, S. K. & Gao, X. L. Bernoulli-Euler beam model based on a modified couple stress theory. *J. Micromech. Microeng.*, **16**, 2355-2359 (2006).

24. Maranganti, R. & Sharma, P. Length scales at which classical elasticity breaks down for various materials. *Phys. Rev. Lett*., **98**, 195504 (2007).

25. Askes, H.; Aifantis, E. C. Gradient elasticity in statics and dynamics: an overview of formulations, length scale identification procedures, finite element implementations and new results. *Int. J. Solids Struct.*, **48**, 1962-1990 (2011).

26. Jiang, Z.; He, J.; Deshmukh, S. A.; Kanjanaboos, P.; Kammath, G.; Wang, Y.; Sankaranarayanan, S. R. S.; Wang, J.; Jaeger, H. M. & Lin, X. M. Subnanometre ligand-shell asymmetry leads to Janus-like nanoparticle membranes. *Nat. Mater.*, **14**, 912-917 (2015).

27. Wang, Y.; Kanjanaboos, P.; Mcbride, S.; Barry, E.; Lin, X. M. & Jaeger, H. M. Mechanical properties of self-assembled nanoparticle membranes: stretching and bending. *Faraday Discuss*., **181**, 325 (2015).

28. Lin, X. M.; Jaeger, H. M.; Sorensen, C. M. & Klabunde, K. J. Formation of long-range-ordered nanocrystal superlattices on silicon nitride substrates. *J. Phys. Chem. B*, **105**, 3353-3357 (2001).

29. Pablo, P. J.; Schaap, I. A. T.; MacKintosh, F. C. & Schmidt, C. F. Deformation and collapse of microtubules on the nanometer scale. *Phys. Rev. Lett*., **91**, 098101 (2003).

30. Schaap, I. A. T.; Carrasco, C.; Pablo, P. J.; MacKintosh, F. C. & Schmidt, C. F. Elastic response, buckling and instability of microtubules under radial indentation. *Biophys. J*., **91**, 1521-1531 (2006).

31. Mahadevan, L.; Vaziri, A. & Das, M. Persistence of a pinch in a pipe. *Europhys. Lett.,* **77**, 40003 (2007).

CHAPTER 6

THERMO-MECHANICAL RESPONSE OF SELF-ASSEMBLED NANOPARTICLE MEMBRANES[§]

6.1 Introduction

Ultrathin membranes composed of metallic or semiconducting nanoparticles capped with short ligand molecules are hybrid materials that have attracted considerable research interests.[1-9] In contrast to other two-dimensional (2D) membranes such as graphene and transition metal dichalcogenides monolayers, nanoparticle membranes can be engineered to achieve unique tunable mechanical, electronic or optical properties, with almost unlimited chemical combinations of inorganic cores and organic ligands. In terms of mechanical properties, these membranes can form large area (tens of microns in diameter) freestanding structures with high Young's moduli (~GPa) and fracture strength.[1,10-12] Previous molecular dynamics simulations imply this remarkable mechanical behavior is mainly contributed by the van der Waals interactions between interdigitated ligands that depends on local ligand structure.[13-18] However, no experimental result exists to validate these simulations by relating the macro-scale mechanical properties to the micro-scale ligand molecule configurations, or to show the mechanical behavior can be tuned by controlling the ligand-mediated interactions between nanoparticles, without the need to change the material's chemical composites.

[§] This chapter is largely based on Wang, Y. *et al.* Thermo-mechanical response of self-assembled nanoparticle membranes. To be submitted (2016).

In this work, we conduct the first experiments to explore this macro-scale and micro-scale relations. Specifically, the thermal-mechanical response of nanoparticle membranes is studied by directly measuring their Young's moduli at elevated temperatures. Consistent with the predictions from simulation, we do observe a decrease of Young's moduli as temperature increases. However, this change is non-reversible during the first annealing cycle, indicting a permanent change of ligand structure which is not predicted by previous simulations.[14,18] Using coarse-grained molecular dynamic simulation, we attribute the irreversible thermo-mechanical behavior to the reorganization of ligand from an initially asymmetric distribution to a more symmetric distribution, while the initial asymmetry comes from the membrane self-assembly process at water-air interface.[19] We then demonstrate that the hysteresis in thermo-mechanical response can be changed by controlling the initial ligand packing density or crosslinking the ligands with electron beam exposure. In addition, the membrane mechanical response was found to depend largely on the environment humidity as water molecules screen interactions between particles. Our work not only provides a more in-depth understanding on how the molecular scale ligand structure between the nanoparticles affects the macroscopic behavior of this material, but also opens up new possibilities to control the mechanical properties of this material by changing the ligand-mediated interaction between the particles.

6.2 Experimental setup

For these experiments, Au nanoparticles with diameters of $(5.2 \pm 0.3nm)$ capped with dodecanethiol ligands were, as before, synthesized using the digestive ripening method[20] described in Chapter 2. The nanoparticles were washed extensively by ethanol for 3 times and re-

suspended in toluene. A volume concentration of 10^{-4} dodecanethiol was back added to the nanoparticle solution, previous results have shown that this ligand concentration is not sufficient to cover the entire nanoparticle surface. To fully cover the nanoparticle surfaces, a higher volume concentration of 5×10^{-4} was added to the washed nanoparticle solution for comparison. In order to make freestanding nanoparticle monolayers, a carbon coated TEM grid (Quantifoil 657-200-CU from Ted Pella) with $2\mu m$ holes was placed on a PTFE substrate, and a $100\mu L$ distilled water droplet was deposited on the substrate covering the TEM grid. Then $10\mu L$ of nanoparticle solution was added to the edge of the water droplet. The nanoparticles immediately climbed to the air-water interface and formed a raft, which further grew and covered the entire surface. The water droplet with nanoparticle monolayer was left to dry for 5-6 hours and the monolayer eventually draped itself onto the carbon grid, forming freestanding monolayers spanning across the holes.

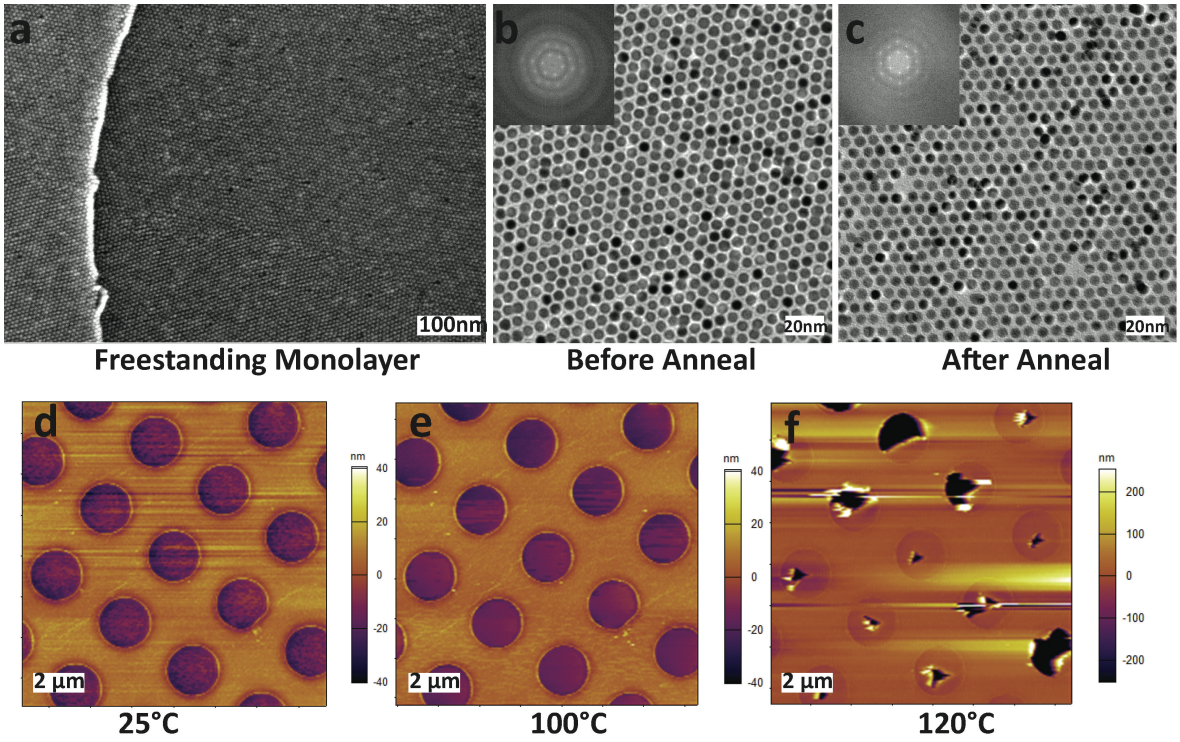

Figure 6.1 (a), SEM image of freestanding nanoparticle monolayer across a 2µm diameter hole

Figure 6.1, continued. on carbon TEM grid. (**b,c)**, TEM image of freestanding nanoparticle monolayer before and after annealing at 80°C, the inset shows FFT of these nanoparticle lattices, the change of lattice constant is not detectable within resolution. (**d-f),** AFM scanning images of nanoparticle monolayers at different temperatures. The monolayer stays intact till 100°C, but starts to rip and fracture at 120°C.

A Carl Zeiss Merlin SEM was used to image the freestanding nanoparticle monolayers down to individual nanoparticle resolution and crystalline structures with ~μm size domains were found (Figure 6.1a). The same SEM was also used to expose freestanding monolayers to an electron beam in order to crosslink the ligands between nanoparticles, which occurs when a large exposure dose is applied. A Tecnai F30 TEM was used to obtain higher resolution images of the nanoparticle monolayers and measure the particle sizes and the interparticle spacing (Figures 6.1b&c). An Asylum MFP3D atomic force microscope (AFM) equipped with AC240 cantilevers was used to obtain tapping mode images and force-indentation curves of the freestanding monolayers (Figures 6.1d-f). A cooler-heater accessory kit was installed on the AFM to change the sample temperature in an enclosed cell. For each temperature step, the sample was left for ~20mins to reach thermal equilibrium before AFM imaging and indentation. The AFM cantilever was calibrated at each temperature step to acquire accurate force-indentation data. AFM indentation and retraction curves were both recorded, and the indentation data were analyzed to obtain the Young's modulus. The stiffness of bare carbon TEM grids without nanoparticle monolayers was also measured and subtracted from the force-indentation curves, thus only force responses from the freestanding monolayers were considered in the analysis.

6.3 Results and Discussion

First, we qualitatively tested the thermal stability of these freestanding membranes. The membrane sample was loaded into an enclosed sample cell in a nitrogen environment, and temperature was systematically varied from 10°C to 120°C. After very gentle indentations (~5nN) on these membranes at each temperature, AFM tapping mode images were recorded to check the integrity of the membrane (Figures 6.1d-f). We found that the freestanding membranes were quite stable after AFM perturbations up to a high temperature of 100°C. Above 100°C, the membranes became fragile and easy to break upon indentation. Most membranes ripped and fractured after 5nN AFM indentation at 120°C (Figure 6.1f). This result indicates that the membranes possess considerable mechanical stability up to 100°C, which is in contrast to previous molecular dynamic (MD) simulation results[13,14] that predicted surface ligand melting at ~20°C and Young's modulus vanishing to zero at ~50-60°C in 3D gold-dodecanethiol superlattices. We suppose that this variation comes from the difference between 3D structures in simulations and 2D monolayers in our experiment where surface effect becomes more important.

To measure the mechanical properties of the membranes more quantitatively, we used AFM probes to indent at the centers of the membrane and recorded the force-indentation data at each temperature. Typical force-indentation of a single membrane is as shown in Figure 6.2a. These force curves show linear behavior at small indentation and nonlinear behavior with higher stiffness towards large indentation. To extract the membranes' intrinsic mechanical properties

from such force curves, we used a previously developed model of a linear elastic disk clamped along the circumference that is subjected to center loading. The force response *F* and indentation depth δ can be related by:[1,10]

$$F = \sigma^{2D}\pi\delta + E^{2D}(q^3R)(\frac{\delta}{R})^3 \tag{6.1}$$

Here σ^{2D} is the pre-stress in the membrane coming from both the fabrication process and clamping at the wall; $R = 1\mu m$ is the radius of the membrane; q is a constant depending on the Poisson ratio ν (q=1.02 in our case where $\nu = 0.34$);[21] E^{2D} is the 2D Young's modulus of the membrane, related to the 3D Young's modulus E by $E^{2D} = E \cdot t$ where $t = 7nm$ is the physical membrane thickness including the diameter of the nanoparticle core and the thickness of the ligand shell. Using this model, we can fit the experimental force-indentation curves to Equation 6.1 and obtain the fitting parameters σ^{2D} and E. When measuring at room temperature (25°C) in dry nitrogen environment, we found $\sigma^{2D} = 0.44 \pm 0.04 N/m$ and $E = 19 \pm 3GPa$. Given the fact that there are no chemical bonds between neighboring nanoparticles and ligands, the high Young's modulus is quite remarkable. This fitting result also suggests the pre-strain in these membranes is $\varepsilon_0 = \frac{\sigma^{2D}}{Et} = 0.3\%$, below the failure strain (~1.6%) of the membranes, as measured previously.[11]

The analysis to obtain the Young's moduli was performed on force-indentation data at different temperatures from 5°C to 90°C (Figures 6.2a&b). At each temperature, ten membranes are measured and averaged. These measurements show that the membrane Young's modulus decreases from ~21GPa at 5°C to ~8GPa at 90°C during heating process, which is almost a 60% decrease. This result is a direct proof that the membrane moduli has a large contribution from the

ligand interactions[13-18] rather than from gold core only, since the van der Waals interaction between gold cores does not change significantly within this temperature range. As the temperature is reduced, the monolayers regained their strength only partially, back to ~12GPa at 10°C, much lower than the initial value before the heating-cooling cycle. This large hysteresis during the heating-cooling cycle is in contrast with previous simulation results that have essentially shown no hysteresis,[14,18] as they predict the temperature induced ligand disorder is completely reversible when temperature is reversed. Thus, the experimentally observed hysteresis in Young's modulus is highly unexpected. However, this hysteresis is not found in the second and subsequent heating-cooling cycle (Figure 6.2c&d), where the modulus-temperature dependence is also less than the first cycle. These results indicate the hysteretic behavior of thermo-mechanical response during the first annealing cycle is related to an irreversible change of ligand configuration in the membrane.

In order to explain this irreversible ligand configuration change, an important fact to note is that the nanoparticles used in the above experiments are extensively washed so the ligand density is not high enough to cover the entire surface of gold nanoparticles. Our recent study on these membranes using grazing incidence small angle X-ray scattering shows a ligand-shell asymmetry develops in the membranes during the self-assembly process.[19] The fact that membranes are formed through a self-assembly process at a water-air interface means that nanoparticle are exposed to two different environments, thus the density of hydrophobic dodecanethiol ligands is intrinsically non-symmetric, *i.e.* ligand density at the air-facing side is slightly higher than the water-facing side. This means that an as-fabricated membrane may not

have thermodynamically most favorable ligand configuration, while ligand rearrangement and reorganization could take place at higher temperatures.

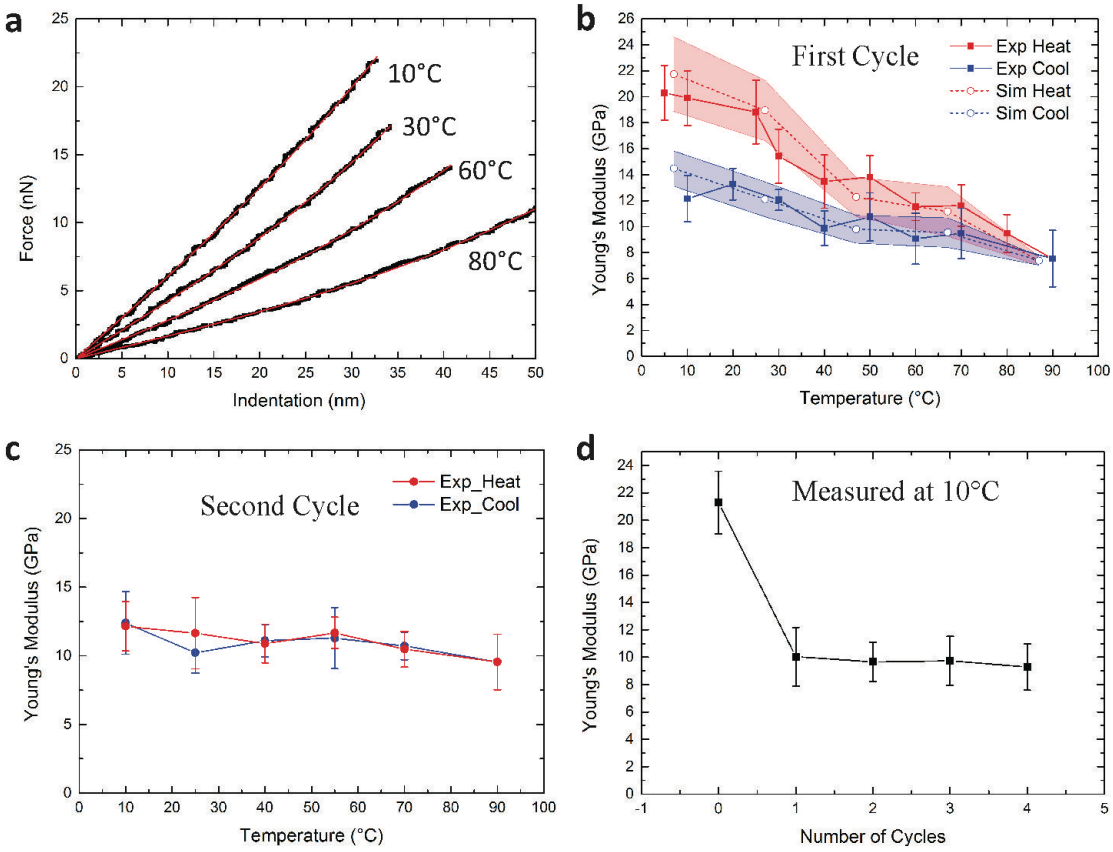

Figure 6.2 (a) Force-Indentation curves of freestanding monolayers at different temperatures from 10°C to 80°C done in dry nitrogen environment, red lines are fittings from Equation 1. (**b)** Change of Young's moduli after the first heating (red) and cooling (blue) cycle, with error bar shows the standard deviation over ~10 samples. The shaded region shows molecular dynamics simulations results with errors, which are scaled by a constant factor to overlay with the experimental curves. (**c**) The monolayer Young's moduli for the second heating-cooling cycle. (**d)** Membrane Young's moduli measured at 10°C after different number of heating-cooling cycles.

We perform coarse-grained molecular dynamics (CGMD) simulations to model the macroscopic mechanical behavior of freestanding nanoparticle membranes. The simulation cell consists of 16 nanoparticles. Monolayers formed of partially ligated nanoparticles with ligand coverage of 0.31

nm^2/ligand, which corresponds to the extensively washed membranes in experiments, were subjected to uniaxial tensile tests under a heating-cooling cycle. The potential energy plot in Figure 6.3a shows the heating-induced change in membrane configurations to energetically (~11.5 kcal/mol/ligand) more stable ones. Young's moduli obtained from the slope of stress-strain curves (Figure 6.3b) at different temperatures, averaged over 8 membrane configurations and scaled by a constant, reproduce the pronounced hysteretic thermal-mechanical behavior observed in experiment (Figure 6.2b**)**.

Analysis of the simulation trajectories reveals collective microscopic rearrangements of nanoparticle ligands that give rise to the hysteretic behavior. As shown in Figure 6.3c, the distribution of ligands in the initial as-prepared membranes is asymmetric due the interfacial self-assembly process used for their preparation, but the low coverage of ligands coupled with ligand mobility at high temperatures allows ligands to reorganize on nanoparticle surface to a near-uniform symmetric distribution. Such rearrangement of ligands reduces the number of interdigitating ligands between nanoparticles by ~5% but on the other hand enhance the extent of interdigitation by ~10% after the first heating-cooling cycle, which results in a large lowering of Young's modulus with increasing temperature. Although some of these non-interdigitating ligands can become interdigitating again during subsequent cooling, the overall number of interdigitating ligands in the final membrane is ~2% less than the as-prepared membrane.

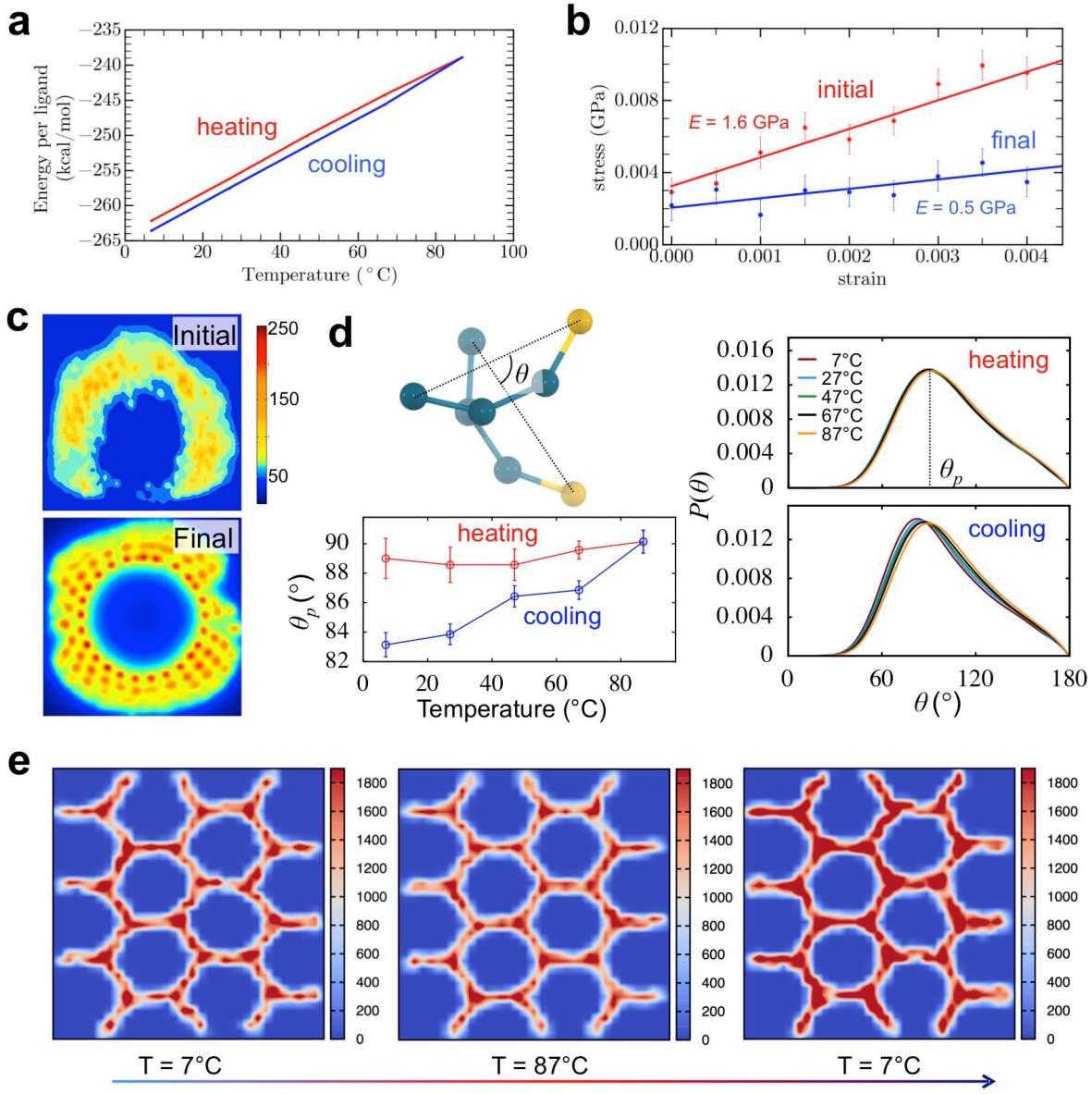

Figure 6.3. Structural evolution of freestanding monolayers during an annealing (heat-cool) cycle as obtained from coarse-grained molecular dynamics simulations. (**a).** Change in potential energy as a function of temperature, and (**b)** significant difference in stress-strain behavior (at strain rate of 2.5×10^{-4}/ns) between the initial and final samples at 7°C. (**c).** Distribution of ligands around a typical nanoparticle before (initial) and after (finial) the heat-cool cycle. (**d**). Angular distribution between the end-to-end vectors of interdigitating ligands (as depicted in the schematic) at different temperatures. In the schematic image, the ligand beads that bind to a nanoparticle are shown in yellow, while others are depicted in blue. (**e).** Density maps showing the change in the number of interdigitating ligands during an annealing cycle.

Despite a decrease in the number of interdigitating ligands, the extent of ligand interdigitation in a membrane after the heating-cooling cycle is found to be ~1% higher than the as-prepared membrane. This surprising result is mostly due to changes in ligand conformation that occur during cooling, where the distribution of angle between their end-to-end vectors (Figure 6.3d) shifts from an initial probable angle of θ_p ~89°-90° to θ_p ~83° at 7°C. The ~6° change in θ_p gives much better contacts among interdigitating ligands, which translates to more robust membranes in the second cycle that display a reversible mechanical behavior (Figure 6.2c and 6.2d) with lowered overall Young's moduli. The transformation of an as-prepared membrane through the heating-cooling cycle is illustrated in Figure 6.3e via color maps that show the extent of ligand interdigitation.

After understanding the micro-scale origin of the hysteresis behavior during first thermal cycle, an interesting question arises as how this hysteresis can be controlled. One way to control the hysteresis behavior during first thermal cycle is to reduce the initial ligand packing asymmetry. This was achieved by adding excess dodecanethiol ligands to the nanoparticle solution, which can increase the ligands packing density around nanoparticles and greatly suppress the ligand-shell asymmetry, in accordance with previous results.[19] Figure 6.4a shows that the hysteresis in moduli-temperature response is much reduced in fully ligated membranes. In addition, these membranes have lower Young's modulus (~40% less) than with lower, initially asymmetric ligand coverage. We believe that this reduction is due to the slightly larger inter-particle spacing and shorter ligand-interdigitation length when nanoparticles are fully packed.

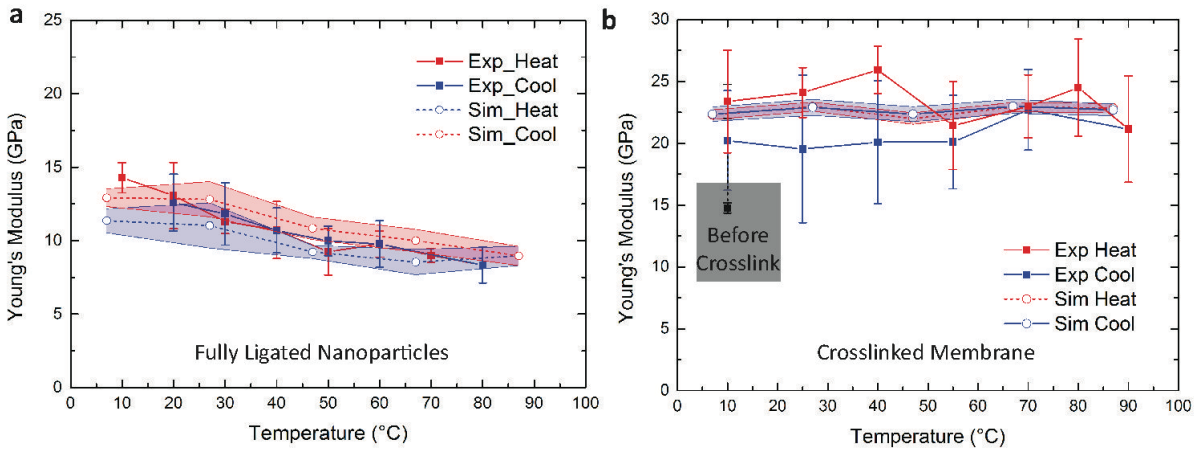

Figure 6.4. Controlling the hysteretic thermal-mechanical behavior. **(a)** The Young's moduli and temperature dependence of a fully ligated nanoparticle monolayer. **(b)** Monolayer Young's moduli before and after crosslinked with electron beam. Shaded regions in these figures are simulation results with error, which are scaled by a constant factor to overlay the experimental trend.

Another method to control the moduli-temperature hysteresis is to constrain ligand rearrangements at higher temperatures. Studies on self-assembled monolayers (SAMS) have shown that electron beams can cause C-H, C-C, and C-S bond cleavage which leads to new C=C bond formation and crosslinks the monolayer.[22] Our previous work has also shown that electron beam exposure introduces strain into the monolayer due to crosslinking.[19,21] With this concept, we exposed a sufficiently large electron beam dose[21] (~25mC/cm^2) to the freestanding membranes at 10 *keV* voltage with SEM. Young's moduli of these membranes before and after exposure were measured in Figure 6.4b, which shows the membrane Young's moduli increased by ~50% after e-beam exposure due to crosslinking of ligands. The cross-linked membranes' Young's moduli were also measured through the heating-cooling cycle, as they stay almost unchanged from 10°C to 90°C with very little hysteresis (Figure 6.4b). This result proves that by crosslinking the ligands, their rearrangements at high temperatures are largely constrained which explains the reduced temperature dependence of Young's moduli.

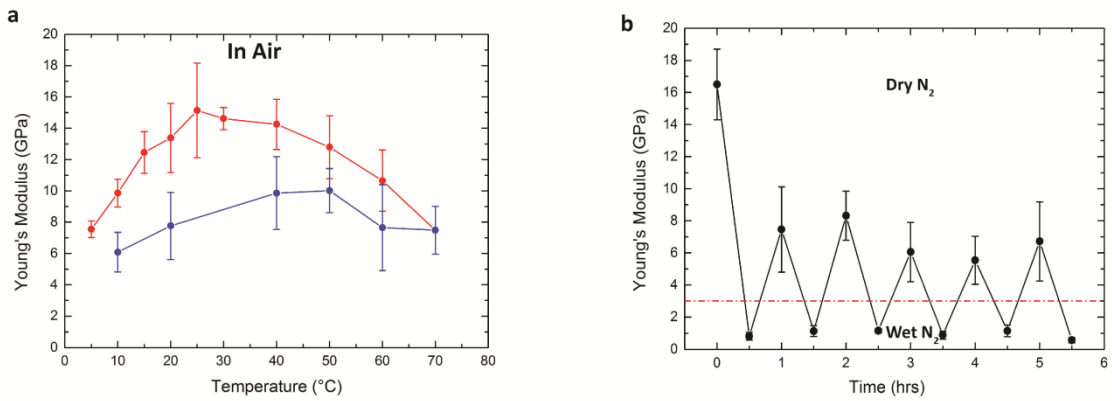

Figure 6.5. (a) Monolayer Young's moduli and temperature dependence measured in ~40% humidity air. (**b)** Monolayer Young's moduli measured at 25°C in switching dry and wet nitrogen environment.

Eventually, given that the van der Waals forces between ligands are related to electromagnetic interactions, a change in the dielectric constant of the surrounding environment should also impact the membrane mechanical properties. Since water molecules have a high dielectric constant of ~80, they will largely screen the interactions between ligand molecules, and reduce the overall monolayer mechanical moduli. To verify this prediction, we measured the Young's moduli of freestanding monolayers in air with ~40% humidity instead of dry nitrogen (Figure 6.5a). The results show a significant drop in modulus below room temperature (~25°C). One possible explanation is the increase of condensation of water vapor on the membrane with decreasing temperature. To prove this, the monolayer moduli were measured while switching from dry nitrogen to "wet" nitrogen. The wet nitrogen, with ~90% humidity, was produced by bubbling dry nitrogen through a container filled with water. The results (Figure 6.5b) show that the monolayer modulus can be controllably and repeatedly weakened by wet nitrogen, while it recovers to a higher value when switched to dry nitrogen (the reason the data in this figure do not recover the initial value is the water molecules trapped in the membranes once wet cannot

evaporate fully during the 30min gap period). Since water molecules have a high dielectric constant of ~80, they will largely screen the interactions between ligand molecules, and reduce the overall monolayer mechanical moduli.

6.4 Conclusion

In summary, we explored the thermal-mechanical responses of freestanding nanoparticle membranes. Their moduli were found to decrease at higher temperatures, but didn't recover to the original value as temperature cools down. Coarse grained molecular dynamics (CGMD) simulations traced the origin of the hysteretic thermal-mechanical behavior to changes in the molecular scale ligand conformation and reorganization. We then demonstrated that the hysteresis in the moduli-temperature dependence can be tuned by controlling the ligand-shell asymmetry or constraining ligand rearrangements with e-beam. Humidity enabled reduction of the membrane moduli via screening ligand interactions was also discovered.

In addition to a better fundamental understanding about ligand interactions in controlling the mechanical properties of nanoparticle membranes, these studies open up new applications as environmental sensing devices. For example, prior work in our lab has shown that the membranes can be used as self-assembled nano-mechanical resonators.[23] As the membranes' stiffness is dependent on temperature, their resonance frequency is also expected to change with temperature, which in turn suggests applications as nano-sized temperature sensors (as long as water vapor condensation can be neglected). Conversely, when temperature is held fixed, the fact

that small amounts of water vapor can change their mechanical properties also makes these membranes potential humidity sensing devices.

6.5 References

1. Mueggenburg, K. E.; Lin, X. M.; Goldsmith, R. H. & Jaeger, H. M. Elastic membranes of close-packed nanoparticle arrays. Nat. Mater. **6**, 656-660 (2007).

2. Cheng, W.; Campolongo, M. J.; Cha, J. J.; Tan, S. J.; Umbach, C. C.; Muller, D. A. & Luo, D. Free-standing nanoparticle superlattice sheets controlled by DNA. Nat. Mater. **8**, 519-525 (2009).

3. Dong, A.; Chen, J.; Vora, P. M.; Kikkawa, J. M. & Murray, C. B. Binary nanocrystal superllatice membranes self-assembled at the liquid-air interface. Nat. Mater. **466**, 474-477 (2010).

4. Talapin, D. V.; Lee, J. S.; Kovalenko, M. V. & Shevchenko, E. V. Prospects of colloidal nanocrystals for electronic and optoelectronic applications. Chem. Rev. **110**(1), 389 (2010).

5. Lee, J. S.; Kovalenko, M. V.; Huang, J.; Chung, D. S. & Talapin, D. V. Band-like transport, high electron mobility and high photoconductivity in all-inorganic nanocrystal arrays. Nat. Nanotech. **6**, 348-352 (2011).

6. Rupich, S. M.; Castro, F. C.; Irvine, W. T. M. & Talapin, D. V. Soft epitaxy of nanocrystal superllatices. Nat. Comm. **5**, 5045 (2014).

7. Liao, J.; Blok, S.; van der Molen, S. J.; Diefenbach, S.; Holleitner, A. W.; Schonenberger, C.; Vladyka, A. & Calame, M. Ordered nanoparticle arrays interconnected by molecular linkers: electronic and optoelectronic properties. Chem. Soc. Rev. **44**, 999 (2015).

8. Kovalenko, M. V.; Manna, L.; Cabot, A.; Hens, Z.; Talapin, D. V.; Kagan, C. R.; Klimov, V. I.; Rogach, A. L.; Reiss, P.; Milliron, D. J.; Sionnest, P. G.; Konstantatos, G.; Parak, W. J.; Hyeon, T.; Korgel, B. A.; Murray, C. B. & Heiss, W. Prospects of nanoscience with nanocrystals. ACS Nano. **9**, 1012 (2015).

9. Boles, M. A.; Engel, M. & Talapin, D. V. Self-assembly of colloidal nanocrystals: from intricate structures to functional materials. Chem. Rev. **DOI**: 10.2021/acs.chemrev.6b00196 (2016).

10. He, J.; Kanjanaboos, P.; Frazer, N. L.; Weis, A.; Lin, X. M. & Jaeger, H. M. Frabrication and mechanical properties of large-scale freestanding nanoparticle membranes. Small **6**, 1449-1456 (2010).

11. Wang, Y.; Kanjanaboos, P.; Barry, E.; Mcbride, S. Lin, X. M. & Jaeger, H. M. Fracture and failure of nanoparticle monolayers and multilayers. Nano Lett. **14**, 826-830 (2014).

12. Wang, Y.; Kanjanaboos, P.; McBride, S. P.; Barry, E.; Lin, X. M. & Jaeger, H. M. Mechanical properties of self-assembled nanoparticle membranes: stretching and bending. Faraday Discuss. **181**, 328-338 (2015).

13. Luedtke, W. D. & Landman, U. Structure and thermodynamics of self-assembled monolayers on gold nanocrystals. J. Phys. Chem. B **102**, 6566-6572 (1998).

14. Landman, U. & Luedtke, W. D. Small is different: energetic, structural, thermal, and mechanical properties of passivated nanocluster assemblies. Faraday Discuss. **125**, 1-22 (2004).

15. Schapotschnikow, P.; Pool, R. & Vlugt, T.J.H. Molecular simulations of interacting nanocrystals. Nano Lett. **8**, 2930-2934 (2008).

16. Salerno, K. M.; Bolintineanu, D. S.; Lane, J. M. D. & Grest, G. S. High strength, molecularly thin nanoparticle membranes. Phys. Rev. Lett. **113**, 258301 (2014).
17. Salerno, K. M.; Bolintineanu, D. S.; Lane, J. M. D. & Grest, G. S. Ligand structure and mechanical properties of single-nanoparticle-thick membranes. Phys. Rev. E **91**, 062403 (2015).

18. Salerno, K. M. & Grest, G. S. Temperature effects on nanostructure and mechanical properties of single-nanoparticle thick membranes. Faraday Discuss. **181**, 339-354 (2015).

19. Jiang, Z.; He, J.; Deshmukh, S. A.; Kanjanaboos, P.; Kamath, G.; Wang, Y.; Sankaranarayanan, K. R. S.; Wang, J.; Jaeger, H. M. & Lin, X. M. Subnanometre ligand-shell asymmetry leads to Janus-like nanoparticle membranes. Nat. Mater. **14**, 912-917 (2015).

20. Lin, X. M.; Jaeger, H. M.; Sorensen, C. M. & Klabunde, K. J. Formation of long-range-ordered nanocrystal superlattices on silicon nitride substrates. J. Phys. Chem. **105**(17), 3353-3357 (2001).

21. Kanjanaboos, P.; Joshi-Imre, A.; Lin, X. M. & Jaeger, H. M. Strain patterning and direct measurement of Poisson's ratio in nanoparticle monolayer sheets. Nano Lett. **11**, 2567-2571 (2011).

22. Zhou, C.; Trionfi, A.; H., J. W. P. & Walker, A. V. Electron-beam-induced damage of alkanethiolate self-assembled monolayers (SAMS): dependence of monolayer structure and substrate conductivity. J. Phys. Chem. C, **114**, 9362-9369 (2010).

23. Kanjanaboos, P.; Lin, X. M.; Sader, J. E.; Rupich, S., Jaeger, H. M. & Guest, J. R. Self-assembled nanoparticle drumhead resonators. Nano Lett. **13**, 2158 (2013).

CHAPTER 7

SUMMARY AND OUTLOOK

This thesis focused on self-assembled Au nanoparticle membranes and their mechanical properties. First of all, I introduced the nanoparticle synthesis and self-assembly techniques whereby freestanding nanoparticle membranes can be fabricated. Secondly, I demonstrated how to introduce in-plane strain in the membranes and obtain their fracture strength by investigating the crack statistics. I found that the membranes exhibit high fracture strength even without crosslinking of the ligands between nanoparticles. In a second set of experiments I exploited the small top-bottom asymmetry of the ligand packing density in the membranes to curl them up into 3D hollow structures we call nano-scrolls. I applied AFM indentation to the hollow nano-scrolls and recorded the force response, which was analyzed using elasticity theory to obtain the bending resistance. Surprisingly, the membranes' bending resistance is ~100 times higher than expected from classical elasticity theory predictions, which we believe comes from the breakdown of this theory when the membrane thickness is approaching the size of individual nanoparticles. Finally, I investigated the thermal-mechanical behavior of freestanding nanoparticle membranes. Temperature and humidity were shown to be key factors that contribute. With the help of molecular dynamic simulations performed in collaboration with reseachers at Argonne, I showed that the macroscopic changes in mechanical behavior can be related to the molecular scale ligand configuration changes.

Knowing the mechanical properties of the nanoparticle membranes, the future outlook is to use this novel, ultrathin material for a range of different applications. The first type of application is

for filtration devices. With ultrahigh surface-to-volume ratio, porous internal structure and tunable capping ligands, these membranes can be used in filtration systems for either liquid or gas. The ~1nm gaps between nanoparticles can allow small molecules to flow through while the capping ligands can be functionalized to block larger ions.[1,2] One major limit to these filtration devices is when mechanical failure takes place under applied pressure. With better understanding of the fracture and failure behavior of these membranes, developed in the thesis, we gain better control over the relevant parameter space.

Another promising application for these ultrathin materials might be for stretchable electronics.[3] Due to their special fracture behavior, where micro-cracks form under stretching instead of long channel cracks, the membranes stay overall mechanically intact and might provide a conducting path even under large strain (~60%). Of course, this requires the membranes to be conductive or semi-conductive at the first place. Recent works by Talapin *et al.* show that high electron mobility in this membranes can be achieved by replacing the capping ligands from non-conductive organic molecules to conductive inorganic ligands.[4,5] The high electron mobility combined with the micro-crack fracture behavior make these all-inorganic membranes a good candidate for stretchable electronics material. Other potential applications include environmental sensors with freestanding membranes as mentioned in Chapter 6.

More importantly, from the fundamental physics aspect, the exciting results from this thesis show that classical continuum elasticity theory may break down when material dimensions reach a new length scale. Although previous works on linear elastic stretching suggest these membranes can be modeled like classical elastic sheets,[7-9] my new experiments show this

comparison is no longer appropriate when considering inelastic stretching (fracture) and bending. The stretching experiment in Chapter 3 shows these membranes fracture into short micro-cracks instead of long channel cracks seen in continuum thin films,[10] possibly caused by ductility between discrete nanoparticles. More interestingly, in Chapter 5 I demonstrate that the bending resistance of these membranes is much higher than predicted from classical elasticity theory, due to the discrete, finite size nature of nanoparticles and possible non-local effects. This break down of classical elasticity is just starting to be in another ultrathin thin film material: graphene.[11] In addition, one distinct advantage of our nanoparticle membranes over other thin film materials including graphene is that: the nanoparticles can be resolved and tracked to analyze the strain and stress in the material. This makes the nanoparticle membranes a perfect system to study elasticity theory at a new length scale where classical continuum elasticity breaks down, as the material dimension approaches the finite size of the constituent units.

7.1 References:

1. He, J.; Lin, X. M.; Chan, H.; Vukovic, L. Kral, P. & Jaeger, H.M. Diffusion and filtration properties of self-assembled gold nanocrystal membranes. *Nano Lett.*, **11**, 2430-2435 (2011).

2. Barry, E.; McBride, S. P.; Jaeger, H. M. & Lin, X. M. Ion transport controlled by nanoparticle-functionalized membranes. *Nat. Comm.* **5**, 5847 (2014).

3. Rogers, J. A.; Someya, T. & Huang, Y. Materials and mechanics for stretchable electronics. *Science* **327**, 1603 (2010).

4. Lee, J. S.; Kavalenko, M. V.; Huang, J.; Chung, D. S. & Talapin, D. V. Band-like transport, high electron mobility and high photoconductivity in all-inorganic nanocrystal arrays. *Nat. Nanotechnol.* 6, 348 (2011).

5. Boles, M. A.; Ling, D.; Hyeon, T. & Talapin, D. V. The surface science of nanocrystals. *Nat. Mater.* 15, 141-153 (2016).

6. Kanjanaboos, P.; Lin, X. M.; Sader, J. E.; Rupich, S. M.; Jaeger, H. M. & Guest, J. R. Self-assembled nanoparticle drumhead resonators. *Nano Lett.* **13**, 2158-2162 (2013).

7. Mueggenburg, K. E.; Lin, X. M.; Goldsmith, R. H. & Jaeger, H. M. Elastic membranes of close-packed nanoparticle arrays. *Nat. Mater.* **6**, 656-660 (2007).

8. He, J.; Kanjanaboos, P.; Frazer, N. L.; Weis, A.; Lin, X. M. & Jaeger, H. M. Frabrication and mechanical properties of large-scale freestanding nanoparticle membranes. *Small* **6**, 1449-1456 (2010).

9. Kanjanaboos, P.; Joshi-Imre, A.; Lin, X. M. & Jaeger, H. M. Strain patterning and direct measurement of Poisson's ratio in nanoparticle monolayer sheets. *Nano Lett.* **11**, 2567-2571 (2011).

10. Chung, J. Y.; Lee, J.-H.; Beers, K. L. & Stafford, C. M. Stiffness, strength, and ductility of nanoscale thin films and membranes: a combined wrinkling-cracking methodology. *Nano Lett*. **11**, 3361-3365 (2011).

11. Blees, M. K.; Barnard, A. W.; Rose, P. A.; Roberts, S. P.; McGill, K. L.; Huang, P. Y.; Ruyack, A. R.; Kevek, J. W.; Kobrin, B.; Muller, D. A. & McEuen, P. L. Graphene Kirigami. *Nature*, **524**, 204-207 (2015).

APPENDIX

A. NANOPARTICLE SYNTHESIS METHODS

A1. The digestive ripening method

Materials

Gold Chloride – $AuCl_3$ (Sigma Aldrich, Cat# 334049)

Didodecyldimethylammonium Bromide – DDAB (Fluka, Cat# 36785)

Sodium Borohydride – $NaBH_4$ (Sigma Aldrich, Cat# 213462)

Dodecanethiol (Sigma Aldrich, Cat# 471364)

Procedure

(a) Rinse two clean glass vials with toluene, fill them with toluene and sonicate. Prepare the following in these 2 vials:

(i) 68mg of $AuCl_3$ (in one vial).

(ii) 208mg of DDAB dissolved in 20mL of toluene (in another vial)

(b) Add DDAB solution to $AuCl_3$, stir and shake the vial to mix the solutions, and sonicate for 30 minutes to dissolve.

(c) While sonicating, prepare a 9.4M solution of $NaBH_4$ by dissolving 1.06mg of $NaBH_4$ into 3mL of deionized H_2O. Shake the solution to dissolve, and wait for 8-9 minutes. Note the $NaBH_4$

can be corrosive and this step should be carried out in the hood. The vial should be capped when weighing.

(d) First, cool down the Au solution by rinsing with cold water. Once cooled, react with 74μL of $NaBH_4$. Make sure that the sample has a stir bar in it, and is spinning when $NaBH_4$ is added. Immediately cap and shake vigorously until the color changes, remember to take out the cap frequently to release the gas. Hydrogen gas is released in the process, so make sure not to cap too tightly. Let the solution sit, while stirring for 1 hour.

(e) Use glass pipets to split the solution into two vials (10mL each). Add 0.8mL of dodecanethiol (the thiol binding is immediate, so no need to shake too long). Then add 10mL of ethanol. Allow the solution to precipitate over night.

(f) In the morning, the gold particles will have precipitated to the bottom of the vial. Remove the top solution, and dry the gold particles under vacuum. Once the remaining solution has been completely removed, re-suspend in 10mL of toluene, and then add 0.8mL of dodecanethiol.

(g) Heat the solutions under reflux for 4 hours (heat narrows the size distribution). Reflux is accomplished by using the long glass vials. Slightly loosen the cap so that gas can leave, and set the temperature to 200°C. Allow the solution to cool to room temperature.

(h) Wash #1. Fill the vial with Ethanol and allow to precipitate overnight. In the morning, the gold particles will have precipitated to the bottom of the vial. Remove the top solution, and dry

the gold particles under vacuum. Once the remaining solution has been completely removed, re-suspend the particles in 10mL of Toluene.

(i) Wash #2. Repeat the step in (h) for the second time.

(j) Wash #3. Repeat the step in (h) for the third time.

(k) At this point, it may be necessary to add an additional amount of dodecanethiol (e.g. to a final volume fraction of 10E-5 to 10E-6) for stable monolayer formation. Ideally, Au nanoparticles can be stored at high concentration in excess thiol.

A2. Citrate reduction in water method

Materials

Gold Chloride – $AuCl_3$, Tannic acid, Citric acid trisodium salt

Procedure

(a) Prepare one 250mL beaker, one 150mL beaker, 4 100mL bottles and one 50mL beaker. Wash with deionized water for several times, and sonicate with deionized water for 10 minutes.

(b) Make 1% gold chloride solution by dissolving 1g of gold chloride into 100g solution in the 100mL bottle, sonicate the bottle till dissolve. Prepare 1% tannic acid solution by dissolving 0.5g

tannic acid into 50g solution in the 100mL bottle. Then prepare 1% citric acid trisodium salt solution by dissolving 1g of trisodium salt into 100g of solution in the 100mL bottle.

(c) Take an 150mL beaker, put 1mL of the 1% gold chloride solution and add deionized water to 80mL, then heat the solution up to 60°C, cover the beaker with parafilm. Take another 50mL beaker and put in 4mL of trisodium salt and controlled volumes of tannic acid, 100μL of tanic acid results in ~13nm particles, while 200μL of tannic acid results in ~10nm particles. Add deionized water to the beaker till 20mL, cover with parafilm and heat to 60°C.

(d) Stir the gold chloride while heated with maximum temperature till boiling. When start stirring, mix the two solutions. After boiled, the solution color should turn to clear red, keep the solution boiling for 10 minutes.

(e) Bath the solution in cold water, change the bathing water for 3 times until the solution cools to room temperature. Then pour the cooled solution into a 100mL bottle.

(f) Take 10 Eppendorf tubes filled with 1mL solutions for centrifuging. Use a speed of 14000rpm and centrifuge for 40 minutes at 20°C.

(g) Take out the water on top of the tubes, be careful not to disturb the bottom and take out as much water as possible. Add 1mL ethanol to each tube and shake till dissolve. Pour all tubes into one bottle and sonicate for 10 minutes.

(h) Add 200μL of dodecanethiol to the bottle and 10mL ethanol to fill the bottle. Wait over night for the solution to precipitate.

(i) Take out the liquid on top of the bottle very carefully, add 20mL ethanol in the beaker to wash the particles, let it precipitate and take out the liquid on top.

(j) Repeat (i) to wash the particles for 2 more times.

(k) Take out the liquid on top of the bottle, add 3-4mL of chloroform into the bottle and sonicate for 10 minutes. The particles will be suspended in chloroform and ready for use.